Geophys. J. Int. (2009) **178,** 921–938 doi: 10.1111/j.1365-246X.2009.04209.x

Importance of bimaterial interfaces for earthquake dynamics and strong ground motion

Gilbert B. Brietzke,[1] Alain Cochard[2] and Heiner Igel[1]

[1]*Department of Earth and Environmental Sciences, Ludwig-Maximilians-Universität, München, Germany. E-mail: brietzke@geophysik.uni-muenchen.de*
[2]*École et Observatoire des Sciences de la Terre, 5 rue René Descartes,* 67084 *Strasbourg Cedex, France*

Accepted 2009 April 13. Received 2009 April 5; in original form 2008 July 23

SUMMARY

We perform a numerical investigation of dynamic ruptures on a bimaterial interface in 3-D with regularized slip-weakening friction and a heterogeneous initial shear stress and discuss the resulting strong ground motion. To isolate effects introduced by the material contrast, we perform pairs of simulations with opposite material orientations. We show that for many parameter sets the dynamics of rupture propagation are significantly influenced by the broken symmetry due to the material contrast during rupture propagation. The resulting slip histories of two events with reversed orientations of the material contrast can deviate such that the emanating waves lead to large differences in peak ground motion (peak ground velocity and peak ground acceleration), even when slip-distribution of the individual events are very similar, and therefore their moment magnitudes are basically identical. We also show that the wrinkle-like slip pulse specific to the bimaterial mechanism can be nucleated naturally from an initially crack-like mode of rupture, when the initial stress allows for large propagation distances. Once such a pulse has been nucleated, it travels at a dominant propagation speed close to the generalized Rayleigh velocity. The dynamic weakening of the fault due to the normal stress alteration during slip allows nucleating ruptures to overcome asperities of low initial shear stress in the preferred direction, which is the direction of displacement on the seismically slower side of the fault. In such situations, the orientation of the material contrast determines rupture extent and therefore the size of the earthquake, potentially by orders of magnitude.

Key words: Numerical solutions; Earthquake dynamics; Earthquake ground motions; Rheology and friction of fault zones.

1 INTRODUCTION

Large faults with a long slip history often separate rocks of dissimilar elastic properties. It has been reported that such bimaterial interfaces exhibit remarkable dynamic properties in the 2-D in-plane case that may be relevant to many issues of earthquake rupture dynamics (Ben-Zion & Andrews 1998). The existence of a pulse mode of rupture, travelling unilaterally along a bimaterial interface at the generalized Rayleigh velocity v_{gr} into the direction of displacement in the more compliant side, has been predicted by a theoretical analysis of Weertman (1980). Andrews & Ben-Zion (1997) confirmed the existence of such wrinkle-like pulse-mode of rupture in numerical calculations. Many aspects of the wrinkle-mode of rupture and sliding along a bimaterial interface have been clarified by various studies (e.g. Adams 1995; Cochard & Rice 2000; Ranjith & Rice 2001). In the 2-D in-plane case, slip along a bimaterial interface generates dynamic changes of normal stress, modifying the local fault strength which, in principle, can generate a unilateral wrinkle-like pulse. This mechanism is present neither in the homogeneous case nor the 2-D antiplane case. It has been shown by Cochard & Rice (2000) that there exists also a bimaterial driven pulse in the opposite direction (direction of displacement in the stiffer side) travelling at the *P*-wave velocity of the softer side, v_P^{slow}. A propagation mode at the slower *P*-wave velocity has been identified by Harris & Day (1997) from a simple model of failure induced slip of a single-point asperity on a friction-free fault. Effects of a low velocity fault-zone structure and multiple fault surfaces have been studied by others (e.g. Harris & Day 1997; Ben-Zion & Huang 2002; Brietzke & Ben-Zion 2006). Theoretical and numerical calculations with rate-dependent friction indicate the bimaterial mechanism to be important for earthquake rupture for ranges of parameters leading to macroscopic and statistical asymmetry of rupture properties while being suppressed for others (e.g. Ampuero & Ben-Zion 2008). It has been shown that the wrinkle-like rupture pulse can persist also in the 3-D case where there is a mixing of the in-plane and antiplane cases (Brietzke *et al.* 2007).

© 2009 The Authors
Journal compilation © 2009 RAS

There are good examples for that the bimaterial mechanism seems to be necessary to properly interpret the observations: asymmetric along strike distribution of aftershocks (Rubin & Gillard 2000; Rubin & Ampuero 2007); asymmetric rock damage across faults of the San Andreas system (Dor *et al.* 2006) and geomorphologic asymmetry across the rupture zones of the North Anatolian fault (NNAF) (Dor *et al.* 2008) have been reported. The uncertainty in the basic physical concepts involved and the constraints of their parameter ranges make it difficult to come to definite conclusions, and indeed, the relevance of this mechanism for natural faulting has also been a subject of controversy recently (e.g. Andrews & Harris 2005; Ben-Zion 2006a).

Here we present results of a numerical investigation of dynamic ruptures with regularized slip-weakening friction on a bimaterial interface with a heterogeneous initial shear stress load in 3-D with a free surface. A heterogeneous stress distribution on a bimaterial interface has been used before by Andrews & Harris (2005) for the 3-D case and by Ampuero & Ben-Zion (2008) for the in-plane 2-D case.

2 MODEL SETUP

We numerically simulate dynamic rupture propagation on a planar fault with regularized slip-weakening friction separating two blocks of dissimilar elastic materials (20% contrast). A sketch of the model is shown in Fig. 1. We introduce Λ as a symbol for the Weertman

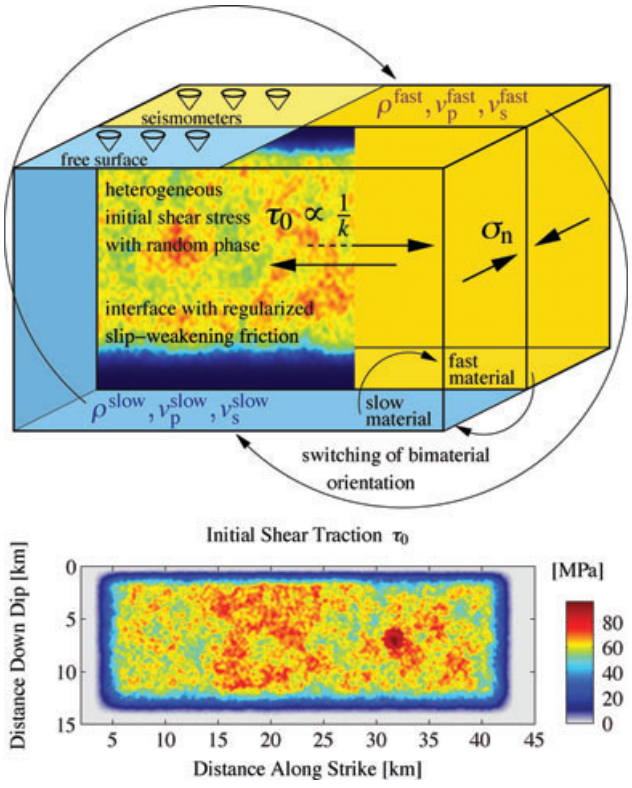

Figure 1. Top panel: sketch of the physical model: bimaterial frictional interface with regularized slip-weakening friction and heterogeneous stress. Each set of parameters is simulated twice, with the material contrast orientation being switched for the second simulation. Bottom panel: example of an initial shear stress distribution. Results of the distribution shown here is presented in Example 2 (Section 3.2) for a single parameter set. The overstressed patch where instantaneous nucleations takes place is visible at about 7 km downdip and 31.5 km along strike in dark red colour.

pulse since slip along a bimaterial interface can, in principle, generate unilateral wrinkle-like Weertman pulses with a unidirectional propagation (Weertman 1980). This direction is often referred to as the *preferred* direction of a bimaterial interface, despite the possible existence of an opposing pulse at v_P^{slow}. We identify the orientation of the material contrast in our simulations by specifying the propagation direction of the mentioned Weertman pulse using Λ_R and Λ_L, subscripts R and L meaning propagation to the right-hand side and to left-hand side, respectively.

2.1 Heterogeneous stress and nucleation

We use a heterogeneous initial shear stress with random phase and amplitude proportional to the reciprocal wavenumber (k^{-1}). Mai & Beroza (2002) find that slip on a fault plane satisfies $D \propto 1/k^{1+H_D}$ with an associated Hurst exponent H_D within the interval of $H_D = [0.5, 1.0]$. For the associated stress field τ_0 the corresponding interval for the Hurst exponent is $H_\tau = [-0.5, 0.0]$. We use $\tau_0 \propto 1/k^{1+H_\tau}$ with $H_\tau = 0$ that corresponds to the upper limit of the range proposed by Mai & Beroza (2002). This value has also been used by Andrews & Harris (2005) and therefore allows for a direct comparison with their results. The distribution is tapered towards zero for wavenumbers close to the Nyquist wavenumber k_{Ny} of our coarsest numerical grid with $\Delta x = 200$ m. The resulting initial shear stress is arbitrarily scaled, and it is smoothly tapered towards the free surface and the model boundaries. We nucleate each event by elevating the initial stress by 15% in a circular patch of 1 km radius around the overall peak-stress of the random distribution.

2.2 Friction and regularization

Frictional sliding along a planar bimaterial interface has been shown to be often ill-posed (Adams 1995; Cochard & Rice 2000; Ranjith & Rice 2001). Regularization is achieved using an experimentally based constitutive law (Prakash & Clifton 1993; Prakash 1998) in combination with classical slip-weakening dependence of friction coefficient [note that slip-weakening alone does not provide regularization—see Cochard & Rice (2000, p. 25 897)]. Shear stress τ in such a system responds gradually to changes in normal stress σ_n. The characteristic differential equation for the shear strength τ^s is given by

$$\dot{\tau}^s = -\frac{|V| + V^*}{L}\left[\tau^s - f_{sw}\max(0, -\sigma_n)\right] \tag{1}$$

with slip velocity V, characteristic slip velocity V^*, characteristic length L and friction coefficient f_{sw}. Friction and slip velocity are vectors and rake rotation is allowed. With this regularized friction law, results in principle converge with grid size reduction (see Cochard & Rice 2000). We use a slip-weakening friction coefficient given by

$$f_{sw} = \begin{cases} f_s - (f_s - f_d)\, D/D_c, & \text{for } D < D_c \\ f_d, & \text{for } D \geq D_c\,. \end{cases} \tag{2}$$

2.3 Numerical method

We use a second-order finite-difference formulation in a staggered grid with traction-at-split-nodes for the implementation of the frictional interface, as it has been introduced by Dalguer & Day (2007). To suppress artificial reflection originated by the finiteness of the numerical model, we use perfectly matched layers (PML) on all

sides of the model except for the side representing the free surface. The PML technique has been adapted to velocity–stress formulations of the elastodynamic wave equations by Collino & Tsogka (2001) in 2-D, and shown to work efficiently in the velocity–stress staggered-grid finite-difference scheme used in this study by Marcinkovich & Olsen (2003). The free surface is implemented using a simple stress-imaging technique at the free surface (Levander 1988).

3 RESULTS

It has been shown by Andrews & Harris (2005) that for a pair of simulations with reversed material orientation (Λ_R, Λ_L) the resulting slip-distribution on the fault may be very similar. Andrews & Harris (2005) also mentioned that the wrinkle-like pulse they observed in their 2-D calculations might have an important effect on the radiated ground motion. Since they have not been able to resolve the wrinkle-like pulse in their 3-D calculations due to computational limits, they could not evaluate its effect on the ground motion, which is the main goal of our study.

We tested for 266 pairs of simulations the influence of the bimaterial mechanism on rupture propagation and final slip as well as on the resulting ground motion. Within this set of simulations, we changed initial shear stress (τ_0) and frictional parameters (f_d, f_s, D_c, L).

We discuss our simulations by showing results of four representative examples in Sections 3.1 (Example 1: similar slip, different ground motion), 3.2 (Example 2: different magnitude), 3.3 (Example 3: wrinkle-like pulse), 3.4 (Example 4: supershear). Each set of parameters is simulated once, and then once again with the material contrast orientation being switched. Each such simulation pair of these four sets of parameters features certain effects that can thus be related to the presence of the material contrast. The 266 pairs of simulations exhibit mixtures of the effects presented in the four representative examples, sometimes less, sometimes more pronounced; those are summarized in Section 3.6.

For characterization of the initial level of shear stress we use the strength excess parameter S, which is defined as

$$S = \frac{\tau_s - \tau_0^{av}}{\tau_0^{av} - \tau_d}, \tag{3}$$

with τ_0^{av} the average initial shear stress in the non-tapered region. Under homogeneous conditions there exists in princple a maximal value of strength excess parameter S above that no transition to supershear can develop (Andrews 1976).

To evaluate differences of final slip we define values for the dissimilarity of final slip and peak slip velocity on the fault, which when the corresponding integrals are discretized become

$$\begin{aligned} \delta D &= \frac{\sum_{i=1}^{N} \left| D_i^{\Lambda_R} - D_i^{\Lambda_L} \right|}{\frac{1}{2}\left(\sum_{i=1}^{N} D_i^{\Lambda_R} + \sum_{i=1}^{N} D_i^{\Lambda_L} \right)}, \\ \delta V_{max} &= \frac{\sum_{i=1}^{N} \left| V_{max_i}^{\Lambda_R} - V_{max_i}^{\Lambda_L} \right|}{\frac{1}{2}\left(\sum_{i=1}^{N} V_{max_i}^{\Lambda_R} + \sum_{i=1}^{N} V_{max_i}^{\Lambda_L} \right)}, \end{aligned} \tag{4}$$

with i the index counting the elements on the fault plane and N the total number of fault elements. We also calculate the correlation coefficient for slip and peak-slip velocity on the fault plane according to the following equations

$$\begin{aligned} C_D &= \frac{\sum_{i=1}^{N} \left(D_i^{\Lambda_R} - \overline{D^{\Lambda_R}} \right) \left(D_i^{\Lambda_L} - \overline{D^{\Lambda_L}} \right)}{\sum_{i=1}^{N} \left(D_i^{\Lambda_R} - \overline{D^{\Lambda_R}} \right)^2 \left(D_i^{\Lambda_L} - \overline{D^{\Lambda_L}} \right)^2}, \\ C_V &= \frac{\sum_{i=1}^{N} \left(V_{max_i}^{\Lambda_R} - \overline{V_{max}^{\Lambda_R}} \right) \left(V_{max_i}^{\Lambda_L} - \overline{V_{max}^{\Lambda_L}} \right)}{\sum_{i=1}^{N} \left(V_{max_i}^{\Lambda_R} - \overline{V_{max}^{\Lambda_R}} \right)^2 \left(V_{max_i}^{\Lambda_L} - \overline{V_{max}^{\Lambda_L}} \right)^2}. \end{aligned} \tag{5}$$

We will look at seismograms and their amplitude spectra at the free surface. All seismograms we will show are low-pass filtered at 2 Hz. Using a grid-spacing of $\Delta x = 100$ m this means that for the slowest wave speed of $v_s^{slow} = 2917\ \mathrm{m\,s^{-1}}$ we have a grid-resolution of 15 points per smallest unfiltered wavelength of 1500 m.

To evaluate the effects on the radiated ground motion on the surface we show maps of peak ground velocity (PGV) and peak ground acceleration (PGA), both calculated after 2 Hz low-pass filtering, and their relative differences with respect to both material orientations (δPGV and δPGA), which are normalized by the average of the value for both orientations PGV^{Λ_R} and PGV^{Λ_L}; they are local parameters at points j on the surface with the same elastic material underneath (this means there is no bias due to the different elastic constants)

$$\begin{aligned} \delta \mathrm{PGV}_j &= \frac{\left| \mathrm{PGV}_j^{\Lambda_R} - \mathrm{PGV}_j^{\Lambda_L} \right|}{\frac{1}{2}\left(\mathrm{PGV}_j^{\Lambda_R} + \mathrm{PGV}_j^{\Lambda_L} \right)}, \\ \delta \mathrm{PGA}_j &= \frac{\left| \mathrm{PGA}_j^{\Lambda_R} - \mathrm{PGA}_j^{\Lambda_L} \right|}{\frac{1}{2}\left(\mathrm{PGA}_j^{\Lambda_R} + \mathrm{PGA}_j^{\Lambda_L} \right)}, \end{aligned} \tag{6}$$

with superscript Λ_R and Λ_L labeling the ground motions of the simulations with its Weertman pulse related preferred directions to the right-hand side and left-hand side, respectively.

We also calculate the moment magnitudes of the synthetic earthquakes using the definition

$$M_W = \frac{2}{3}\left(\log\left(\frac{M_0}{[\mathrm{Nm}]} \right) - 9.1 \right), \tag{7}$$

with defining the seismic moment M_0 at the material interface as

$$M_0 = \frac{2\mu_{fast}\mu_{slow}}{\mu_{fast} + \mu_{slow}} \sum_{i=1}^{N} D_i \Delta x^2, \tag{8}$$

with $\mu_{fast/slow}$ being the shear modulus of the fast and slow side, respectively, D_i slip at fault element i, and Δx^2 the fault element area in our uniform regular grid. Since we calculate the seismic moment using the same definition for all of our events with a fixed material contrast the principal ambiguity of the seismic moment on a material interface (Ampuero & Dahlen 2005) is not relevant to the differential effects we discuss in this study.

In the following, we also show distributions of rupture propagation velocity v_r. We retrieve values for the propagation velocity by calculating the inverse of the smoothed gradient of rupture arrival times (first arrival or peak arrival, as indicated).

The ranges of parameters of our simulations are summarized in Table 1. A full table listing all parameter sets and random realizations of all 266 simulations is given in the Supporting Information (SI 17).

In principle a large regularization parameter L reduces the dynamic bimaterial effect and a large slip-weakening distance D_c reduces the slip-wekaning effect. The choice of regularization parameter $L = (0.1, 0.2)$ was done by trial and error, such that the

© 2009 The Authors, *GJI*, **178,** 921–938
Journal compilation © 2009 RAS

Table 1. Range of tested parameters.

Parameter	Value or value range
Numerical method	Finite-differences
Grid type	Staggered Cartesian grid
Grid-spacing Δx	100 m
Size of physical domain	20 km × 44 km × 20 km
Density fast material ρ^{fast}	2900.0 kg m^{-3}
Wave velocities fast material $v_{\text{S}}^{\text{fast}}$, $v_{\text{P}}^{\text{fast}}$	3500.0, 6000.0 m s^{-1}
Density slow material ρ^{slow}	2416.7 kg m^{-3}
Wave velocities slow material $v_{\text{S}}^{\text{slow}}$, $v_{\text{P}}^{\text{slow}}$	2916.7, 5000.0 m s^{-1}
Size of the fault model $y \times z$	44 km × 20 km = 880 km^2
Type of friction	Regularized slip-weakening
Static friction coefficient f_{s}	0.75, 0.77, 0.8
Dynamic friction coefficient f_{d}	0.4 to 0.7 in steps of 0.1
Characteristic slip velocity V^*	1 m s^{-1}
Characteristic length L	0.1, 0.2 m
Critical slip distance D_{c}	0.2, 0.3 m
Ranges of initial shear stress τ_0	[20,80],[26,80], MPa
(amplitude varies randomly	[40,80],[53,80], MPa
within each range)	[60,80] MPa
Resulting inverse strength excess S^{-1}	[0,1.1]
Initial normal stress σ_{n_0}	100 MPa
Size of nucleation zone $\varnothing_{\text{nuc}}$	2 km
Initial shear stress of nucleation patch	+15%
Resulting moment magnitudes M_{W}	5.3−7.2

bimaterial is not suppressed whereas allowing numerically stable results, and $D_{\text{c}} = (0.2, 0.3)$ is chosen such that earthquakes generated do not exceed a maximum simulation time of 30 s for the realizations we tested whereas also allowing numerically stable results.

To identify robust features we decrease the numerical grid-spacing in selected parameter cases. In those cases, we do not modify the original random realization but interpolate the initial shear stress to the refined grid-spacing [see also discussion in Section 4 and example given in the Supporting Information (SI 15)].

In the following, we discuss stable features present in our 266 pairs of simulations (including the four example cases). Ideally, one should quantify the results in a statistical sense, but we have only one individual random realization per set of physical parameters.

In Section 3.1, we discuss an example where final slip on the fault is very similar for both orientations of a simulation pair (Λ_{L}, Λ_{R}), but the ground motion differs a lot. In Section 3.2, we discuss an example where final slip on the fault and moment magnitude differ a lot between both orientations of a simulation pair (Λ_{L}, Λ_{R}), resulting in huge differences in ground motion. In Section 3.3, we discuss an example where at first a superimposed, finally a distinct wrinkle-like pulse of slip is generated for one material contrast orientation (Λ_{R}), letting the rupture front propagate essentially at the generalized Rayleigh velocity, whereas no such pulse is generated for the reversed setup (Λ_{L}). Here the difference of final slip and moment magnitude is moderate, whereas the difference in ground motion is large. In Section 3.4, we discuss an example where we have the generation of a supershear rupture front propagating to one side, a subshear rupture front to the opposite direction for both material contrast orientations (Λ_{L}, Λ_{R}). This example demonstrates how supershear propagation can be supported or prevented depending on the orientation of the material contrast and how a secondary pulse of rupture can travel behind the supershear rupture front travelling at the generalized Rayleigh velocity.

3.1 Example 1: similar slip, different ground motion

Here we discuss an example where final slip on the fault is very similar for both orientations of the simulation pair (Λ_{L}, Λ_{R}), whereas the ground motion differs substantially.

The parameters are summarized in Table 1. Here $L = 0.2$ m, $D_{\text{c}} = 0.3$ m, $f_{\text{s}} = 0.8$, $f_{\text{d}} = 0.5$, initial shear stress varies randomly between 40 and 80 MPa (tapered to zero towards the edges), inverse of strength excess $S^{-1} = 0.4$, $\Delta x = 100$ m.

The initial shear stress is the same for both simulations with reversed orientation of the material contrast. The rupture is nucleated at about 11.5 km downdip and 24 km along strike by an instantaneously overstressed patch ($\varnothing_{\text{nuc}} = 2$ km around the peak value of initial stress). The actual distribution of initial shear stress is shown in the Supporting Information (SI 1).

The distributions of final slip D for the pair of simulations with switched material orientation (top, Λ_{L} and bottom, Λ_{R}) are displayed in Fig. 2. There is considerable visual similarity. We calculate the correlation coefficient of final slip $C_D = 0.99$, the slip dissimilarity value $\delta D = 9\%$ (eq. 4), and the moment magnitudes M_{W} for both events $M_{\text{W}}^{\Lambda_{\text{R}}} = M_{\text{W}}^{\Lambda_{\text{L}}} = 6.91$, which show that distributions of final slip in this example are indeed very similar. After 10 s already 96% of total final slip in the Λ_{R}-case and 100% of total final slip in the Λ_{L}-case are accumulated so the duration of both events are also comparable.

Slip history on the fault is illustrated in Fig. 3 with distributions of slip velocity at four instances in time for both material contrast orientations (Λ_{L}, Λ_{R}). One can recognize that in this specific example rupture propagates faster to its preferred direction in both cases (Λ_{L}, Λ_{R}). Also the amplitudes of slip velocity at the tip of the crack differ between the two simulations with reversed material contrast orientations. Hence, despite the similarity of final slip (see Fig. 2) rupture history on the fault is significantly altered when switching materials. The correlation coefficient and the dissimilarity value for both distributions of peak slip velocity is $C_V = 0.72$ and $\delta V_{\text{max}} = 14\%$, (eqs 4 and 5). Distributions of peak slip velocity and

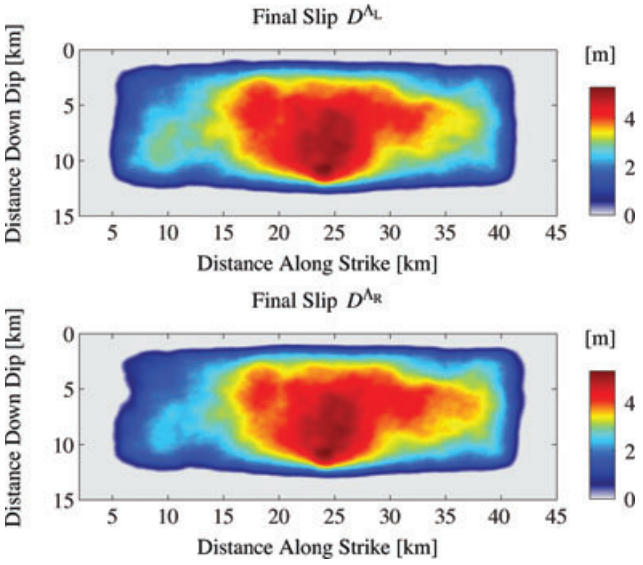

Figure 2. Distributions of final slip for both material orientations (top, Λ_{L} and bottom, Λ_{R}) of Example 1 (similar slip, different ground motion). The correlation coefficient between both distributions of slip is $C_D = 0.99$, slip dissimilarity value, as defined in eq. (4), $\delta D = 9\%$, and the moment magnitudes are identical: $M_{\text{W}}^{\Lambda_{\text{R}}} = M_{\text{W}}^{\Lambda_{\text{L}}} = 6.91$.

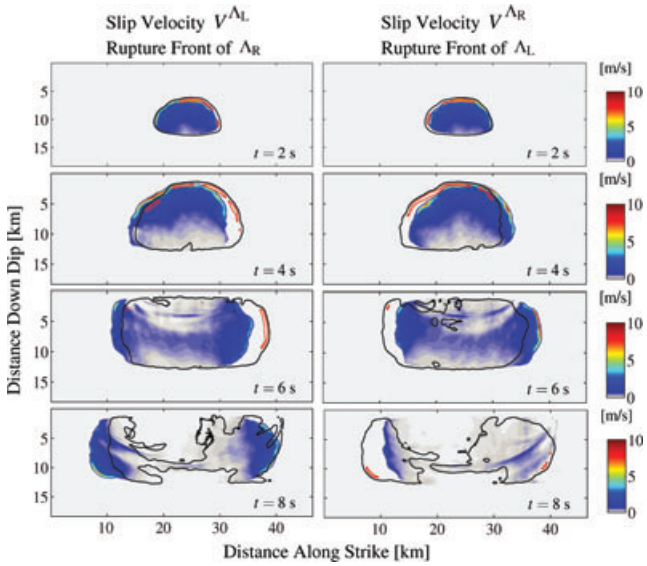

Figure 3. Time evolution of the rupture for Example 1, showing snapshots of slip velocity for four instances in time for both material orientations (left panel, Λ_L, and right panel, Λ_R). To better identify differences between both panels, the red and back lines on each panel correspond to the other panel (reversed orientation); the black contour marks the rupture front (of the reversed orientation), the red one shows regions of high slip velocity (of the reversed orientation). In both cases the rupture is enhanced (higher amplitude and larger propagation velocity) in the preferred direction.

distributions of rupture propagation velocity [both shown in the Supporting Information only (SI 2 and SI 3)] manifest a significant bimaterial effect onto the slip history on the fault.

The example under discussion demonstrates that the rupture history on the fault is controlled both by the distribution of initial shear stress and the bimaterial mechanism. Since the distribution of peak slip velocity V_{max} and propagation velocity v_r for both orientations Λ_L and Λ_R as well as the snapshots of slip velocity for both cases (Fig. 3) would be identical with no material contrast, we infer that the bimaterial effect contributes significantly to the slip history on the fault.

The resulting peak ground motion of Example 1 is shown in Fig. 4. Although the Λ_L case shows a large directivity in PGV as well as in PGA, the directivity is less obvious and not simply reversed for the Λ_R case. In the Λ_L case the area of large PGV and PGA is left of the epicentre at about 18 km along strike, whereas in the Λ_R-case the relevant ground motion is spread over larger portions along the fault. The maximum peak value of ground motion appears in the Λ_L-case and is about 2.3 m s^{-1} peak velocity. We identified its origin with an area of high initial shear traction close to the free surface. This patch of the fault produces also large ground motion in the Λ_R-case, but less pronounced due to its dynamically unfavoured direction. Additionally there is significant ground motion to the right of the epicentre in the Λ_R-case. The area of highest relative difference of peak ground motion is close to the fault at 36 km along strike with values of δPGV $\approx$ 110% and δPGA $\approx$ 140%. The rupture propagation velocity below this area of large ground motion difference is close to the generalized Rayleigh velocity for the Λ_R-case [see Supporting Information (SI 3)].

In Fig. 5, we show seismograms and velocity amplitude spectra at station S_1 (see Fig. 4) located at 36 km along strike, 2 km off fault on the slow sides, for both material contrast orientations (Λ_R, Λ_L). The seismograms are low-pass filtered at 2 Hz. As it can be seen in Fig. 4 this station is located where δPGV $\approx$ 100% and δPGA $\approx$ 130%. For both orientations the signals exhibit a duration of about 10 s where most shaking takes place within a time-window of about 3−13 s. This time-window resembles basically the duration time of the whole event ($\approx$10 s). However, a larger amplification of the signal can be seen in the Λ_R-case within a time-window of 3−8 s than for the Λ_L-case. Therefore, the seismograms exhibit a considerable change in ground motion amplitudes for the reversed orientations of the material contrast. The difference is especially large for the fault normal component of velocity (factor of 3) and acceleration (factor of 6) at station S_1: $\max[v_x^{\Lambda_R}] \approx 3\max[v_x^{\Lambda_L}]$ and $\max[a_x^{\Lambda_R}] \approx 6\max[a_x^{\Lambda_L}]$, whereas the difference in final displacement is negligible for all three components (d_x, d_y, d_z).

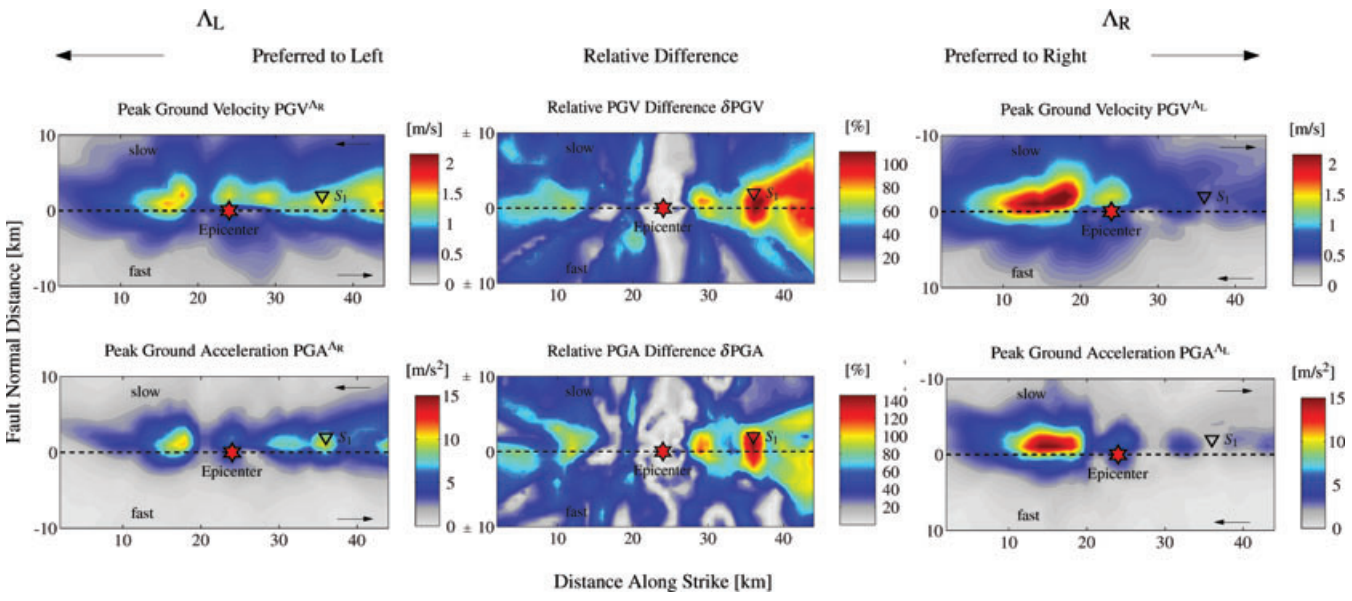

Figure 4. Peak ground motion maps of Example 1 for both material contrast orientations (Λ_L, Λ_R). The epicentre is marked by the red star, the location of a virtual seismometer S_1 is marked by a black triangle, its seismograms being shown in Fig. 5. Note that for the Λ_L-case the fault-normal axis is reversed for easier comparison, hence the slower side is always at the top for all six panels.

© 2009 The Authors, *GJI*, **178,** 921–938
Journal compilation © 2009 RAS

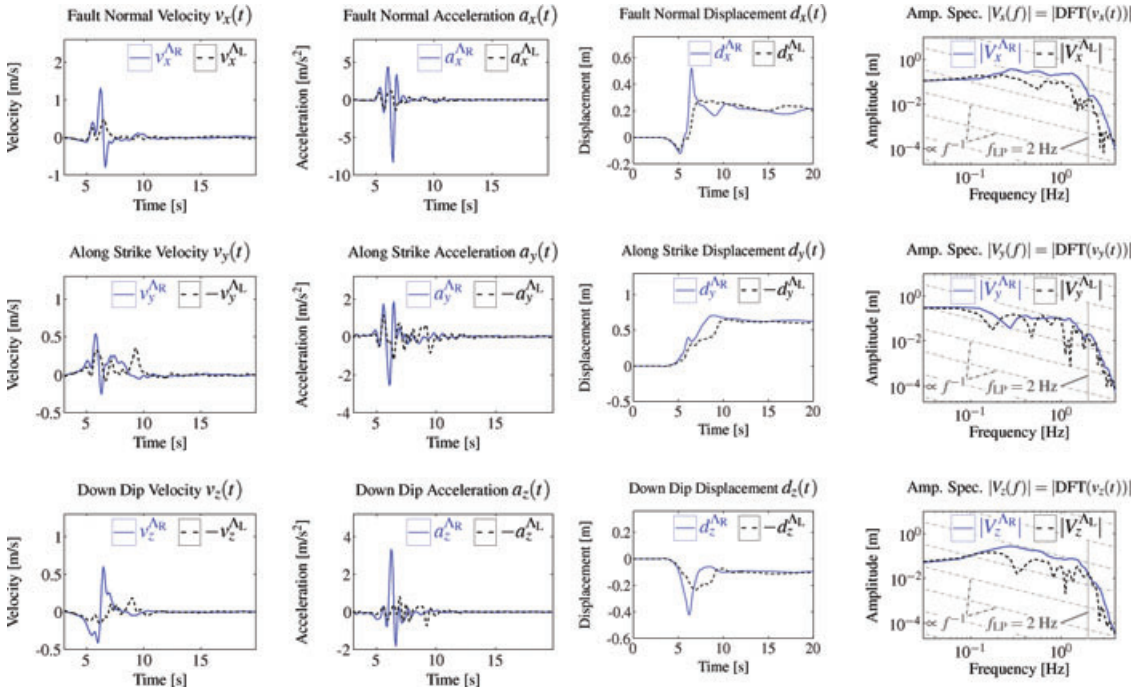

Figure 5. Seismograms and velocity amplitude spectra of Example 1 at stations S_1 for both material contrast orientations (Λ_R, Λ_L). The seismograms are low-pass filtered at 2 Hz. One can see a considerable difference in ground motion when switching materials. The difference is especially large for the fault normal component of velocity (factor of 3) and acceleration (factor of 6) at this station: $\max[v_x^{\Lambda_R}] \approx 3\max[v_x^{\Lambda_L}]$ and $\max[a_x^{\Lambda_R}] \approx 6\max[a_x^{\Lambda_L}]$, whereas the difference in final displacement is negligible for all three components (d_x, d_y, d_z). Note that the difference in the amplitude spectra is significant down to about 0.2 Hz, which is seismologically resolvable!

Final slip of Example 1 ($D = D(y,z)$) is not enough to characterize the wavefield ($v(x, y, z, t)$, $\sigma(x, y, z, t)$) that emanates during the rupture propagation since it contains no information on the time-dependent evolution of the fault. A better fingerprint appears to be peak slip velocity $V_{\max}$ (see SI 2) since it contains some information on the time-evolution of slip as a function of the time-derivative of slip.

We ascertain that the seismic radiation differs substantially between both orientations of the material contrast even though slip on the fault is in general very similar. This possibility was mentioned previously by Andrews & Harris (2005). The large differences in strong ground motion are due to very different slip histories on the fault. Since in our model those can only be different due to the presence of the material discontinuity, this suggests the bimaterial effect to be important for earthquake hazard.

3.2 Example 2: different magnitude

We proceed to an example in which final slip on the fault and moment magnitude differ considerably between both orientations of the simulation pair (Λ_L, Λ_R), resulting in very large differences in ground motion.

The parameters are summarized in Table 1, with specific parameters of $L = 0.2$ m, $D_c = 0.3$ m, $f_s = 0.8$, $f_d = 0.56$, $\Delta x = 100$ m, the range of initial shear stress $\tau_0 = 40 - 80$ MPa (tapered to zero towards the edges), with a resulting inverse strength excess $S^{-1} = 0.39$.

The initial shear stress is the same for both simulations with reversed orientation of the material contrast. The actual distribution for this example is the one shown in Fig. 1 bottom panel. Rupture is nucleated at about 7 km downdip and 31.5 km along strike by an instantaneously overstressed patch ($\varnothing_{nuc} = 2$ km around the peak value of initial stress) visible in dark-red colour.

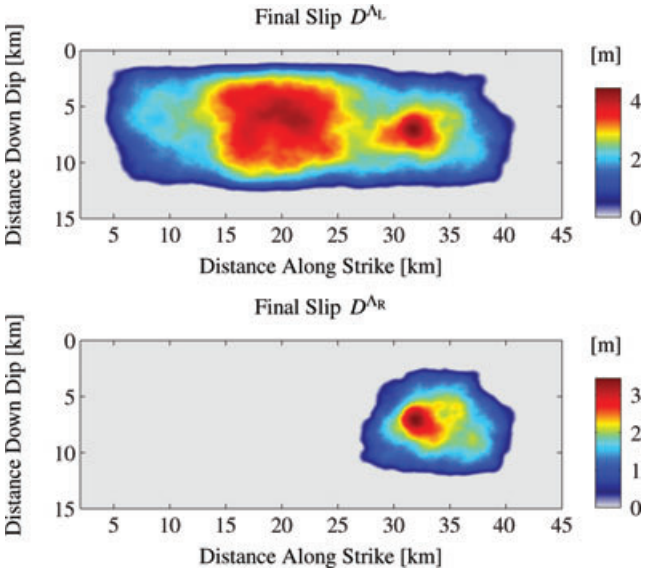

Figure 6. Distributions of final slip for both material orientations (top, Λ_L and bottom, Λ_R) of Example 2 (different magnitude). The correlation coefficient for both distributions of slip $C_D = 0.38$, the slip dissimilarity is $\delta D = 139\%$ and the moment magnitudes differ by half a unit: $M_W^{\Lambda_R} = 6.32$, $M_W^{\Lambda_L} = 6.82$.

In Fig. 6, we show the distribution of final slip D for the pair of simulations with switched material orientation (top, Λ_L and bottom, Λ_R).

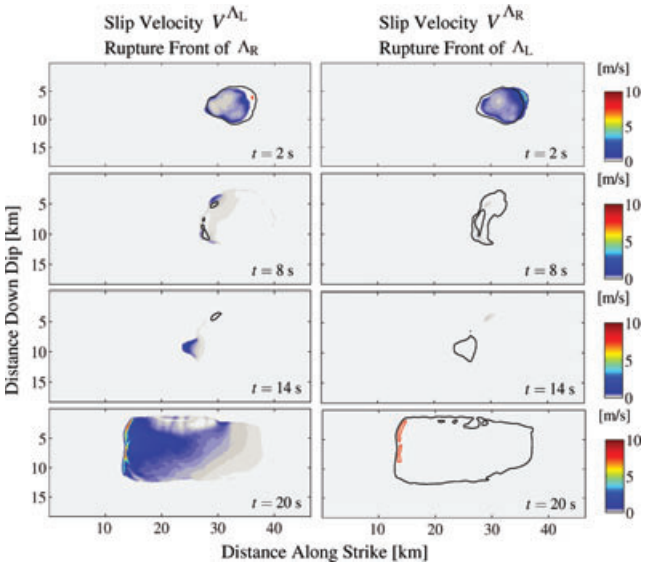

Figure 7. Time evolution of the rupture for Example 2, showing snapshots of slip velocity for four instances in time for both material orientations (left-hand panel, Λ_L, and right-hand panel, Λ_R). The black contour marks the rupture front of the reversed orientation, the red one shows regions of high slip velocity of the reversed orientation.

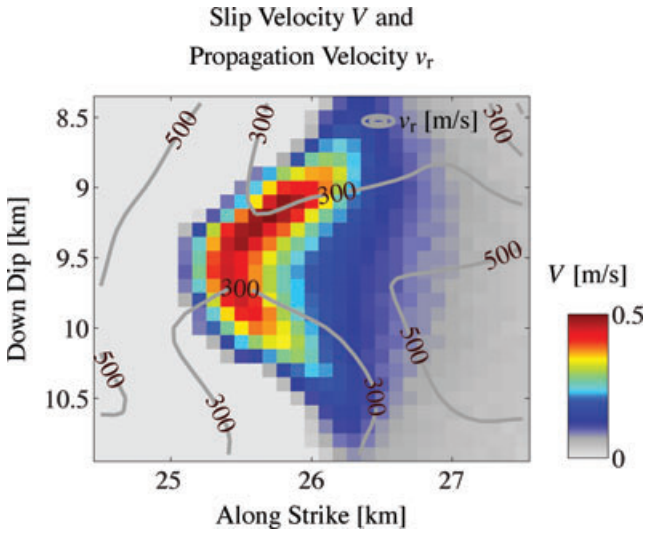

Figure 8. Slip velocity (colour-coded) and propagation velocity calculated from first arrival times (contour) of Example 2 Λ_L-case at $t = 12$ s (compare with Fig. 7, left side, third panel from top).

The correlation coefficient of final slip $C_D = 0.38$, the slip dissimilarity value $\delta D = 139\%$ (eq. 4), and the moment magnitudes for both events are $M_W^{\Lambda_R} = 6.32$ and $M_W^{\Lambda_L} = 6.82$. The distributions of final slip in this example are thus very different.

In Fig. 7, we compare the evolution of slip velocity on the fault for the Λ_L- and Λ_R-case at four instances in time.

One can see that at $t = 2$ s rupture has a slightly higher amplitude and larger propagation velocity in its preferred direction for the Λ_R-case when comparing to the Λ_L-case. At $t = 8$ s and $t = 14$ s there are only tiny slipping patches remaining for the Λ_R-case whereas in the Λ_L-case considerable slipping patches can be recognized. In the Λ_R-case rupture dies out and no slip is remaining at $t = 20$ s. Fig. 8 shows a detail of slip velocity at the moment of minimal slip velocity of the Λ_L-case with additional contours showing the propagation velocity as contour lines.

The snapshot is taken at the moment when in the Λ_L-case rupture slowly overcomes a region of relatively low initial shear stress around 5–10 km downdip and 24–28 km along strike and then speeds up and amplifies in the region of large initial shear stress around 14–24 km along strike (see Fig. 1 bottom panel), and it finally ruptures the entire fault in its preferred direction (Λ_L).

Thus, the bimaterial mechanism helps to overcome an asperity of low initial shear stress initiating a secondary event along the fault in its preferred direction, whereas in the case of reversed material contrast orientation (Λ_R-case) it cannot. The correlation coefficient for the distributions of peak slip velocity and the dissimilarity value of the peak slip velocity distributions are $C_V = 0.07$ and $\delta V_{max} = 41\%$ (eq. 4). Peak slip velocity for Example 2 is shown in the Supporting Information (SI 4). A region with a comparatively small peak slip velocity ($V_{max}^{\Lambda_L} \leq 1\ \mathrm{m\,s^{-1}}$) can be identified at around 25−26 km along strike in the Λ_L-case. This region has low initial shear stress (see Fig. 1 bottom panel). As aforementioned, rupture stops at this obstacle in the Λ_R-case. In the Λ_L-case the region with low initial shear stress can be overcome although slip velocity is less than $1\ \mathrm{m\,s^{-1}}$ and propagation velocity (calculated from arrival times) reaches a minimum value of $v_r^{min} \approx 315\ \mathrm{m\,s^{-1}}$ (see Fig. 8).

Obviously the resulting peak ground motion shows huge differences between the two material contrast orientations (Λ_L, Λ_R). In Fig. 9, we show PGV^{Λ_L} and PGA^{Λ_L} (left side), PGV^{Λ_R} and PGA^{Λ_R} (right side), and δPGV, δPGA (centre). The maximum relative difference in PGV and PGA is almost 190%, the highest possible values being 200% (see eq. 6). As mentioned earlier, in the Λ_L-case we discovered the initiation of a secondary event. This secondary event makes the peak ground motion an order of magnitude of amplitude different (remember the difference in moment magnitude M_W is half a magnitude). The secondary event propagates mainly in the Λ_L-direction and hence has a very strong directivity to the Λ_L-direction. We present seismograms at stations S_1 and S_2 in the Supporting Information (SI 5 and SI 6) (see their locations in Fig. 9).

A characteristic of a Weertman pulse travelling along a bimaterial interface is its propagation velocity $v_r \approx v_{gr}$, the generalized Rayleigh velocity. Fig. 10 shows the rupture propagation velocity for Example 2.

For the Λ_L case (top panel of Fig. 10) the rupture propagation velocity v_r is, in 9% of the total slipping area, close to the generalized Rayleigh velocity ($v_r = [v_{gr} - 6\%, v_{gr}]$). These areas show up in blue colour shading and are an indicator for the Weertman pulse significantly contributing to the rupture dynamics. In both cases most of the fault ruptured with a velocity slower than the generalized Rayleigh velocity, as indicated by the grey shaded regions (94% for Λ_R and 83% for Λ_L). We find there is indication for a superimposed Weertman pulse in Example 2 for the Λ_L-case.

The shown example demonstrates the bimaterial effect to be important in the entire subshear velocity range. First, the bimaterial mechanism is efficient in a range of very slow propagation velocities, giving the ability to overcome asperities of low initial shear stress. Second, there is indication that for an appropriate state of initial shear stress, as in the the Λ_L-case of the given example, and after a sufficiently large propagation distance, features typical for the Weertman pulse (e.g. sharpening behaviour at the rupture front with large slip velocities, and a propagation velocity close to the generalized Rayleigh velocity), nucleate naturally from the initially slow event as a superimposed part of the rupture. The large

© 2009 The Authors, *GJI*, **178,** 921–938
Journal compilation © 2009 RAS

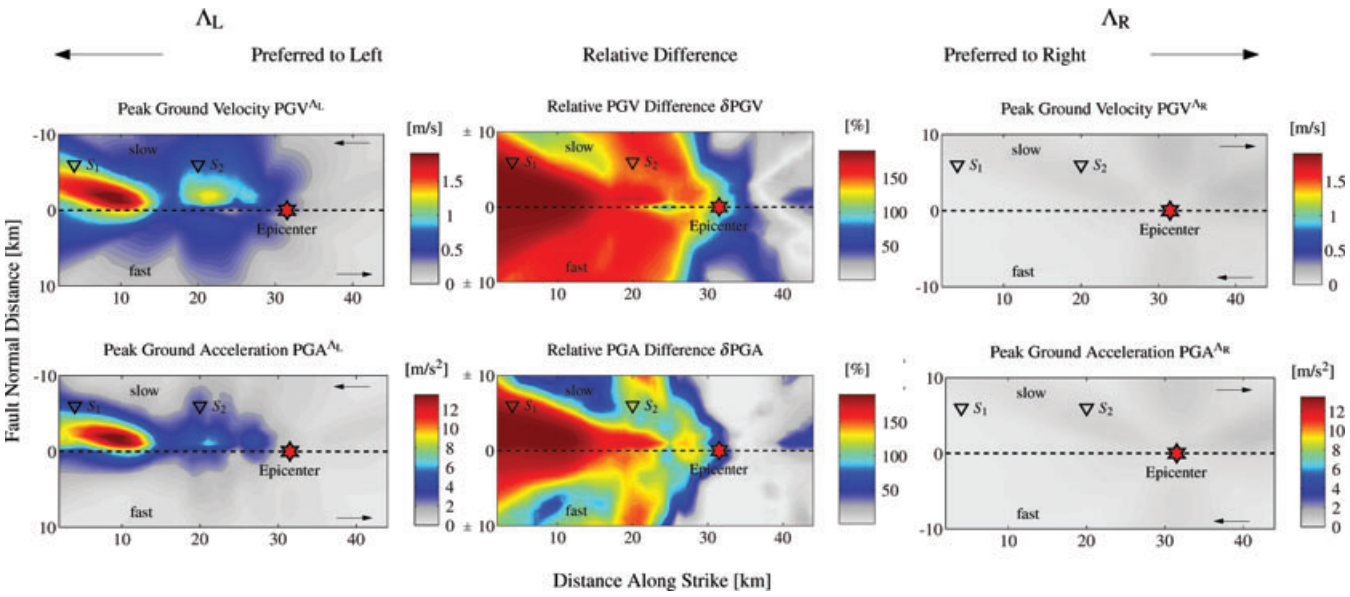

Figure 9. Peak ground motion maps of Example 2 for both material contrast orientations (Λ_L, Λ_R). The epicentre is marked by the red star, the locations of two virtual seismometers S_1, S_2 are marked by black triangles, their seismograms being shown in the Supporting Information (SI 5 and SI 6).

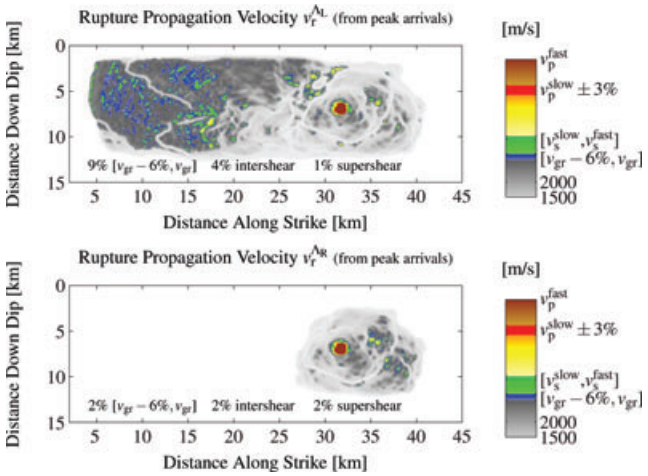

Figure 10. Rupture propagation velocity calculated from the smoothed gradient of peak arrival times for both material orientations of Example 2. For the Λ_L case (top panel) the rupture propagation velocity v_r is, within 9% of the total slipping area, close to the generalized Rayleigh velocity ($v_r = [v_{gr} - 6\%, v_{gr}]$). These areas show up in blue colour shading and are an indicator for the bimaterial mechanism significantly contributing to the rupture dynamics. The instantaneous nucleation patch shows up as a dark red region.

macroscopic difference in this example suggests that the fault is close to a critical state at key parts of the fault where rupture propagation is on the verge of dying or propagating, the bimaterial mechanism being the incident that tips the scale. The resulting peak ground motion is orders of magnitude different for the Λ_L and Λ_R cases. Thus, we can infer that the bimaterial mechanism is important for earthquake dynamics, strong ground motion and earthquake hazard.

3.3 Example 3: wrinkle-like pulse

In this example we show that even a distinct Weertman pulse can nucleate naturally in the presence of heterogeneous stress and slip-weakening friction. Once such a pulse is generated it can more efficiently overcome low-stress regions whereas propagating more or less constantly close to the generalized Rayleigh velocity. The pulse is generating large amplitudes in the emanated wavefield at relatively high frequencies.

The parameters are summarized in Table 1, with specific parameters of $L = 0.2$ m, $D_c = 0.3$ m, $f_s = 0.8$, $f_d = 0.48$, initial shear stress varies randomly between 26 and 80 MPa (tapered to zero towards the edges), inverse of strength excess $S^{-1} = 0.27$, $\Delta x = 100$ m. The initial distribution of shear stress on the fault plane and the resulting distributions of final slip are shown in the Supporting Information (SI 7 and SI 8). The slip distributions provide a correlation coefficient of $C_D = 0.94$ and a slip dissimilarity value of $\delta D = 28\%$. In comparison with the total amount of slip on the fault some additional slip that is present in the Λ_R-case is rather small.

In Fig. 11, we compare the evolution of slip velocity on the fault for the Λ_L- and Λ_R-case at four instances in time.

In the early stage of the rupture ($t = 2$ s) the rupture propagates in a crack-like manner. Then, stopping phases are initiated at the tapered regions at the boundaries (top side first, then bottom and left side) ($t = 4.5$ s). After that, rupture propagates in both cases (Λ_R, Λ_L) to the right side, essentially as a pulse ($t \geq 7$ s). The rupture front of the Λ_L-case propagates much slower than in the Λ_R-case. At time steps $t = 7$ s and $t = 9.5$ s rupture develops towards a distinct pulse in the Λ_R-case with large slip velocity, whereas in the Λ_R-case it is slowly getting smaller.

The correlation coefficient for both distributions of peak slip velocity is $C_V = 0.47$, the dissimilarity value of the peak slip velocity distributions $\delta V_{max} = 27\%$ (eq. 4). Further details are shown in the Supporting Information (SI 9). In Fig. 12, the rupture propagation velocity is shown for both material contrast orientations.

In the Λ_R-case (bottom panel of Fig. 12) the rupture propagation velocity v_r is, within 23% of the total slipping area, close to the generalized Rayleigh velocity ($v_r = [v_{gr} - 6\%, v_{gr}]$). The colour map is constructed such that these areas show up in blue. The predominantly blue-shaded portion of the fault suggests that the Weertman-type of slip pulse is part of the solution. In the Λ_R-case we gather the evidence that there is a superimposed wrinkle-like

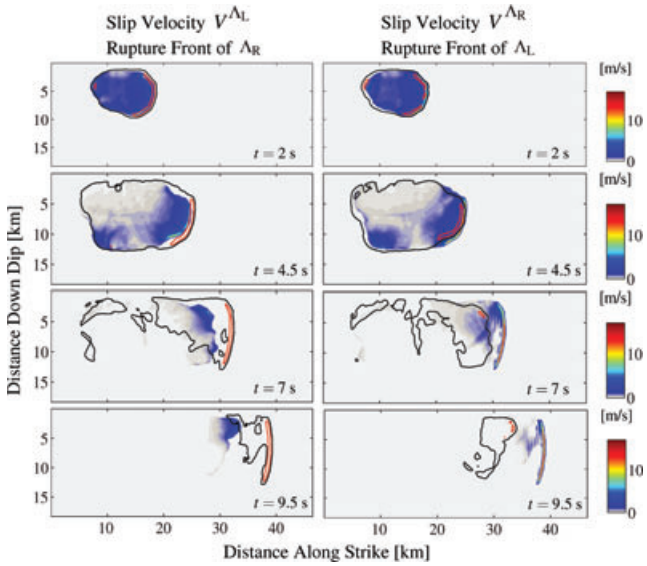

Figure 11. Time evolution of the rupture for Example 3 (wrinkle-like pulse), showing snapshots of slip velocity for four instances in time for both material orientations (left panel, Λ_L, and right panel, Λ_R). The black contour marks the rupture front of the reversed orientation, the red one shows regions of high slip velocity of the reversed orientation. The Λ_R-case features a sharp and distinct pulse.

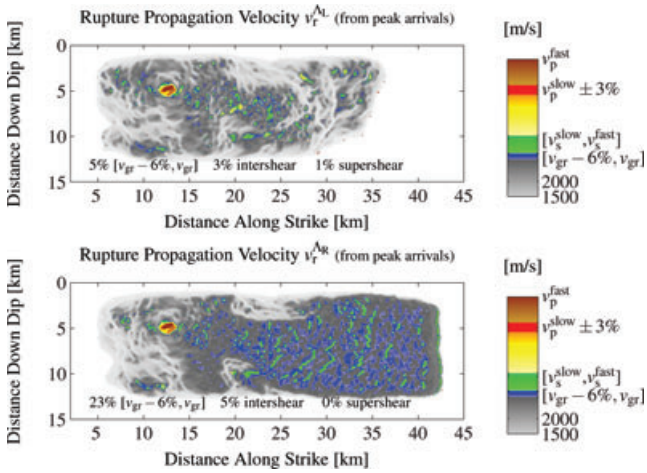

Figure 12. Rupture propagation velocity of Example 3 calculated from the smoothed gradient of peak arrival times of the rupture. The instantaneous nucleation patch shows up as a dark red region with an unrealistically high propagation velocity. For the Λ_R case (bottom panel), the rupture propagation velocity, v_r, is, within 23% of the total slipping area, close to the generalized Rayleigh velocity ($v_r = [v_{gr} - 6\%, v_{gr}]$). These areas show up in blue colour shading and are an indicator that the Weertman-type of slip pulse is part of the solution.

pulse between 18 and 30 km distance along strike and a more or less distinct wrinkle-like pulse from 30 to 41 km distance along strike. In the Λ_L-case the rupture propagation velocity reaches intershear velocity but stays sub-Rayleigh in 91% of the slipping fault area.

The large differences of Λ_L- and Λ_R-case in slip velocity and propagation velocity suggest a large difference in ground motion at the surface for Example 3. Maps of peak ground motion and their differences, for Example 3, are displayed in Fig. 13.

The relative difference values of ground motion (as defined in equation 6) are slightly above 140% for PGV as well as for PGA. The setup of initial shear stress of Example 3 lets the rupture propagate mainly to the right for both material contrast orientations (Λ_L, Λ_R). Therefore a setup induced directivity might be expected in the maps of peak ground motion (Fig. 13) for both cases. In fact in the Λ_R-case we can note a huge directivity. For the Λ_L-case, on the contrary, the potential directivity does not really show up. Here the preferred direction of the bimaterial interface (Λ_L) is opposing the favouring due to the setup, and the ground motion looks much more symmetric than in the Λ_R-case.

Seismograms and spectra at station S_2 (see Fig. 13 for the location) are displayed in Fig. 14. This correspond to a location with δPGV $\approx 110\%$ and δPGA $\approx 125\%$. At this station the duration of shaking for both orientations is within a time-window of slightly above 5 s. However in the Λ_R-case there is a large concentration of energy in the acceleration and velocity at about $t = 8 \pm 1$ s that can be referred to the arrival of the superimposed (at the rupture tip) or rather distinct wrinkle-like pulse. Nevertheless slip is strongly evolving afterwards ($t \geq 10$ s) and final slip is reached at about 14 s. The spectra show that at this location the expected amplitude decay does not meet the $V(f) \propto f^{-1}$ relation, especially for the Λ_R-case.

Additionally we present seismograms and spectra at station S_1 (see Fig. 13 for the location) with δPGV $\approx 50\%$ and δPGA $\approx 90\%$ in the Supporting Information (SI 10).

Although not in the region of highest relative differences, station S_2 in Fig. 14 (as well as station S_1 in SI 10) exhibit considerable differences in the wavefield generated by the two reversed material configurations. The wrinkle-like slip pulse generates large peak velocities and accelerations with a strong directivity. The large accelerations of the fault normal components are especially remarkable (see Fig. 14). The example demonstrates that the phenomenon of the Weertman pulse can become important in earthquake dynamics as well as strong ground motion.

3.4 Example 4: supershear

Under the conditions of relatively high initial shear stress, hence cases where inverse of strength excess S^{-1} is relatively large, we have some cases where rupture becomes supershear. In some cases the bimaterial inhibits the development of supershear rupture in the preferred direction, whereas it supports supershear rupture in the opposite propagation direction. Here we discuss an example in which the rupture propagation velocity becomes supershear over a large portion of the fault.

The parameters are summarized in Table 1, with specific frictional parameters of $L = 0.2$ m, $D_c = 0.2$ m, $f_s = 0.8$, $f_d = 0.52$, $S^{-1} = 0.62$, $\Delta x = 100$ m, initial shear stress varies randomly between 26 and 80 MPa, the actual distribution is shown in the Supporting Information (SI 11).

For both cases (Λ_R and Λ_L) rupture breaks the entire fault; final slip is shown in the Supporting Information (SI 12). The correlation coefficient of final slip is $C_D = 0.98$, the slip dissimilarity value is $\delta D = 11\%$ (eq. 4) and the moment magnitudes M_W for both events are $M_W^{\Lambda_R} = 6.99$ and $M_W^{\Lambda_L} = 7.01$. The distributions of final slip in this example are thus similar.

As we did in the previous examples, we illustrate slip history on the fault with distributions of slip velocity at four instances in time for both material contrast orientations (Λ_L, Λ_R) of Example 4 in Fig. 15.

Rupture initially propagates as an enlarging crack-like rupture mostly slower than the generalized Rayleigh velocity. One can recognize that in each case rupture propagates slightly faster to their

© 2009 The Authors, *GJI*, **178,** 921–938
Journal compilation © 2009 RAS

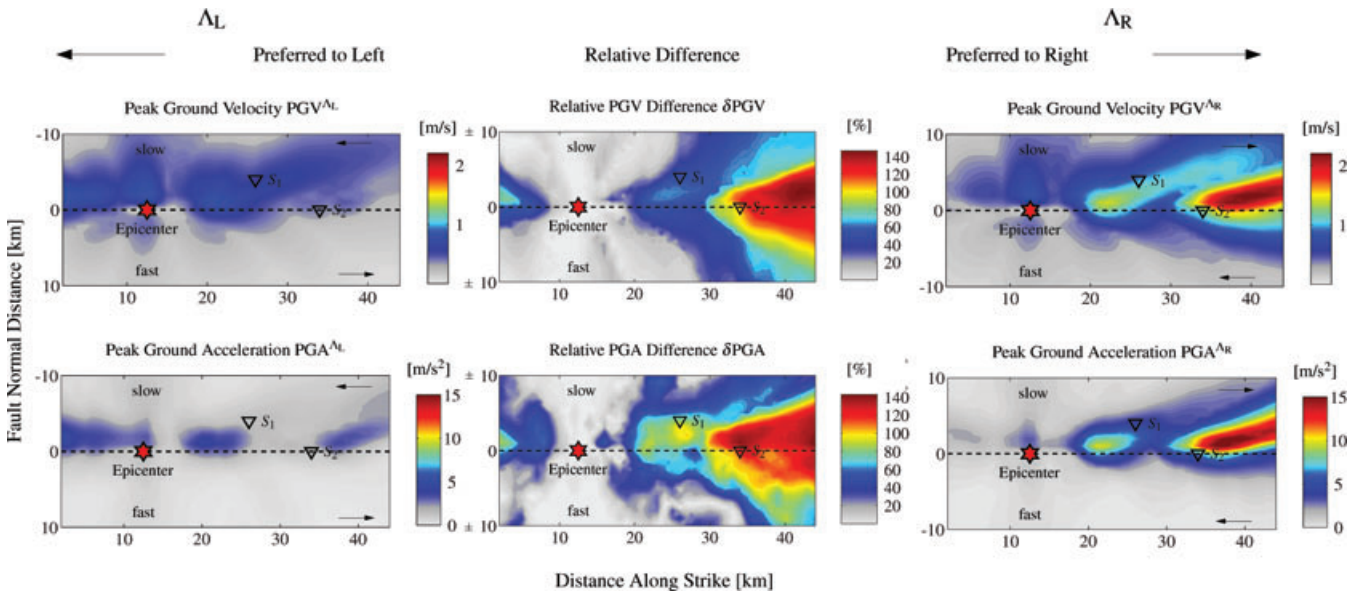

Figure 13. Peak ground motion maps of Example 3 for both material contrast orientations (Λ_L, Λ_R). The epicentre is marked by the red star, the locations of two virtual seismometers S_1 and S_2 are marked by black triangles, their seismograms being shown in Fig. 14 for S_2 and in the Supporting Information for S_1. As expected from the large differences in peak slip velocity and propagation velocity (Fig. 12) one can see that maximum PGV^{Λ_L} and maximum PGV^{Λ_R} differ by almost a factor of 3 and maximum PGA^{Λ_L} and maximum PGA^{Λ_R} differ by more than a factor of 3. Although PGV^{Λ_R} and PGA^{Λ_R} provide a very strong directivity to the right, ground motion in the Λ_L-case is distributed with less directivity.

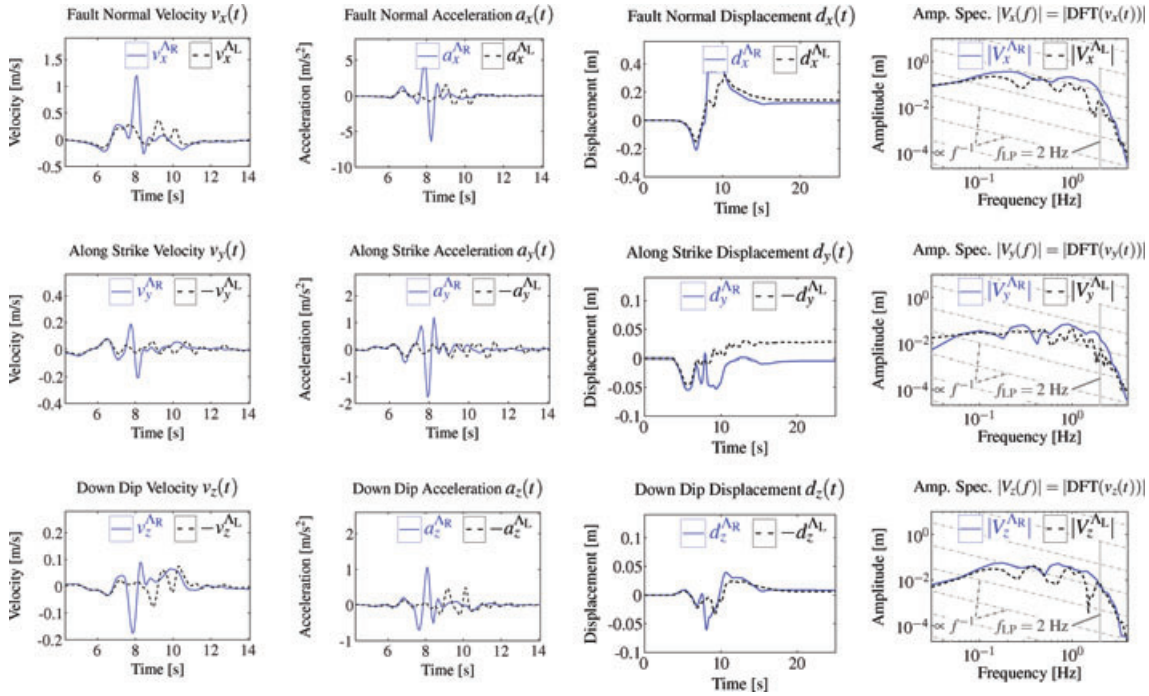

Figure 14. Seismograms and velocity amplitude spectra at station S_2 of Example 3, which is located directly on the fault for the Λ_R and Λ_L case. The seismograms are low-pass filtered at 2 Hz. As can be seen in Fig. 13, this is a station with relative differences: $\delta PGV \approx 110\%$ and $\delta PGA \approx 125\%$. The seismograms show a similar shaking duration of about 5 s, but the signals in the Λ_R-case are more concentrated in a small time-window around $t = 8$ s than in the Λ_L-case.

preferred direction in the early phase of the rupture (until $t \approx 4$ s). Afterwards, the rupture front heading to the left quickly becomes supershear in both cases. The region where supershear propagation is triggered can be related to a large region of relatively high initial shear stress. Although rupture becomes supershear in the Λ_L-case, the propagation phase that holds the peak value of slip velocity ($V_{max}^{\Lambda_L}$) remains mostly at the generalized Rayleigh velocity or the intershear-range. In the Λ_R-case peak slip velocity travels essentially just behind the first arrival of the rupture. The distribution of peak slip velocity is shown in the Supporting Information (SI 13).

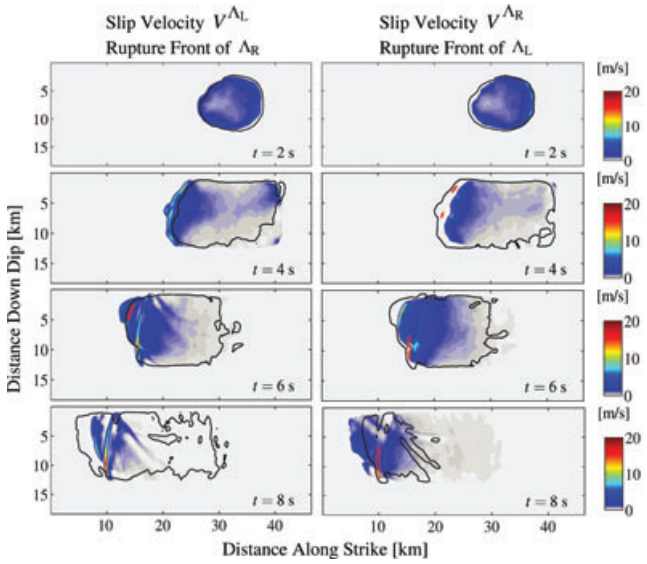

Figure 15. Time evolution of the rupture for Example 4 (supershear), showing snapshots of slip velocity for four instances in time for both material orientations (left panel, Λ_L, and right panel, Λ_R). The black contour marks the rupture front of the reversed orientation, the red one shows regions of high slip velocity of the reversed orientation. Both cases (Λ_L and *LR*) become supershear. However, unlike the Λ_R-case, in the Λ_L-case the peak amplitude travels far behind the supershear first arrival (left panel).

The correlation coefficient for both distributions of peak slip velocity is $C_V = 0.56$, the dissimilarity value of the peak slip velocity distributions $\delta V_{\max} = 17\%$ (eq. 4). Again, slip is much more similar, when comparing the Λ_L- with the Λ_R-case, than distributions of peak slip velocity.

Fig. 15 demonstrates that the rupture history on the fault can be considerably influenced by the bimaterial mechanism also under high-stress condition (small strength excess parameter S). In the previous examples (1−3), we noted that the bimaterial mechanism potentially speeds up rupture propagation in the preferred direction. Here we can remark that when the conditions on the fault are such that rupture can become supershear, the bimaterial mechanism may delay the arrival of peak slip velocity such that a secondary rupture propagation phase behind a supershear rupture tip holds the peak values, or it can even suppress supershear propagation. In Fig. 16, we show rupture propagation velocities of Example 4 calculated from peak arrival times as well as propagation velocity calculated from first arrival times.

The slip history on the fault shown in Fig. 15 also becomes evident in the plots of the rupture propagation velocity. In the Λ_L-case the peak travels close to the generalized Rayleigh velocity over 27% of the fault (Fig. 16 bottom left), whereas supershear propagation is also initiated for 7% of the fault area (Fig. 16 top left). However, the difference in the propagation velocities from first arrivals and from peak arrivals (compare Fig. 16 top left with bottom left) show that despite the supershear propagation at the rupture tip a secondary rupture phase with higher slip velocity propagates behind the rupture tip. In the Λ_R-case the propagation velocities calculated from first arrival times and from peak arrival times agree much more than in the Λ_L-case, which reveals the fact that no considerable secondary rupture phase travels behind the rupture front. In the Λ_R-case more than 20% of the fault rupture at a propagation velocity in the supershear range (see Fig. 16 right side). However there is only little indication (red colour) for a rupture phase travelling at the velocity of the slower *P*-wave velocity v_P^{slow}.

In Fig. 17, peak ground motion on the surface for Example 4 is shown. The peak amplitudes of velocity and acceleration are unrealistically high in this example ($PGV_{max}^{\Lambda_L} \approx 5\ m\,s^{-1}$, $PGA_{max}^{\Lambda_L} > 30\ m\,s^{-12}$). However, this is mostly due to a small patch with very high slip velocities just below the surface at about 18−19 km along strike distance in both cases (Λ_L, Λ_R).

Seismograms and spectra at station S_1 (see location in Fig. 17) are presented in the Supporting Information (SI 14). The differences between the simulations with reversed orientation are remarkable.

3.5 General stable features

Just after triggering the instantaneous nucleation patch, rupture starts propagating as essentially classical crack-like ruptures in the the sub-Rayleigh velocity range. In many cases with a small inverse strength excess S^{-1} the initial shear stress does not allow for

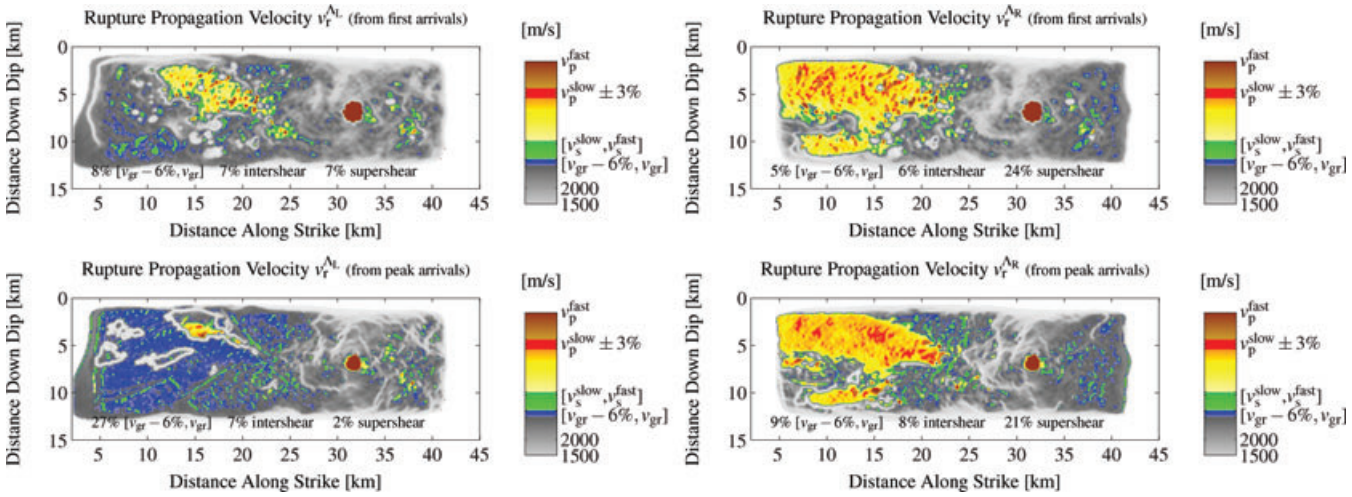

Figure 16. Rupture propagation velocity of Example 4. For the Λ_L-case (left side) and for the Λ_R-case (right side) rupture propagation velocity calculated from the smoothed gradient of first arrival times (top) and calculated from the smoothed gradient of peak arrival times (bottom). The two cases with reversed material contrast show significant difference in propagation velocities. The differences between propagation velocities calculated from first (top) and peak arrivals (bottom) are larger for the Λ_L-case (left side).

© 2009 The Authors, *GJI*, **178,** 921–938
Journal compilation © 2009 RAS

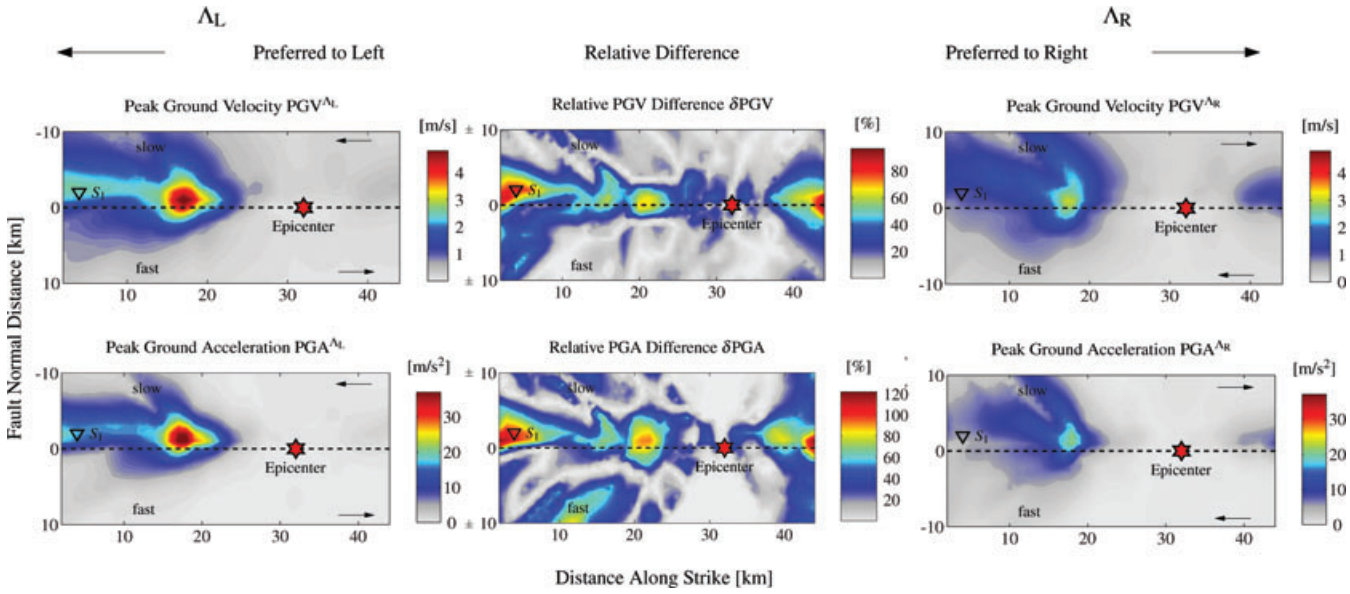

Figure 17. Peak ground motion maps of Example 4 for both material contrast orientations (Λ_L, Λ_R). The epicentre is marked by the red star, the location of a virtual seismometer S_1 is marked by a black triangle, its seismograms being shown in the Supporting Information (SI 14). In this example peak amplitudes of velocity and acceleration are unrealistically high close to 2 km off fault distance, 4 km along strike distance ($PGV_{max}^{\Lambda_L} \approx 5\ m\,s^{-1}$, $PGA_{max}^{\Lambda_L} > 30\ m\,s^{-12}$). The largest relative difference shows up above the left vicinity of the fault around station S_1.

large propagation distances and large propagation velocity. In these cases rupture stays in the sub-Rayleigh propagation mode over the entire event duration. In other cases the inverse of strength excess S^{-1} is larger and initial shear stress allows for larger propagation velocities. In those cases the rupture often develops superimposed wrinkle-like pulses as part of the rupture or, after larger propagation distances, even exhibits predominant wrinkle-like pulses of slip. Although slip can be very similar when comparing the simulations with reversed material contrast orientation, ground motion differ substantially even when both cases (Λ_L and Λ_R) are sub-Rayleigh. On average, the differences in peak ground motion within a pair of simulations with reversed material contrast are larger in the cases when a superimposed or distinct wrinkle-like pulse of slip is present. For very large S^{-1} we find cases where propagation velocity becomes supershear. We find that the material contrast supports supershear propagation in the unfavoured propagation direction, whereas it shows the tendency of preventing ruptures from becoming supershear in the preferred direction. This may be related to the existence of an additionally favoured mode, that is antipodal to the preferred direction of the Weertman pulse (Λ-direction) and travelling at the velocity of the slower P-wave (see Cochard & Rice (2000) for details). However, only a few cases exist within the tested parameter range for which the supershear propagation is in a significant area percentage ($\geq$5%) close to the velocity of the slower P-wave v_P^{slow}. In our simulations we have cases with differences of moment magnitudes of up to $\Delta M_W = 1$ within one pair of simulations with reversed material contrast orientation but same parameters.

3.6 Results of 266 simulation pairs

The four examples in Sections 3.1 (Example 1: similar slip, different ground motion), 3.2 (Example 2: different magnitude), 3.3 (Example 3: wrinkle-like pulse), and 3.4 (Example 4: supershear) show that a heterogeneous initial shear stress on a bimaterial frictional interface governed by regularized slip-weakening friction can produce a wide range of rupture propagation modes within the tested parameter space. We first visually inspected 266 simulation pairs, then defined objective criterion for the occurrence of the following modes of rupture propagation:

(i) sub-Rayleigh propagation;
(ii) superimposed wrinkle-like slip pulse propagating into the preferred direction;
(iii) predominant or distinct wrinkle-like pulse of slip propagating into the preferred direction;
(iv) intershear propagation;
(v) supershear propagation;
(vi) supershear propagation close to the P-wave velocity of the slower medium propagating to the non-preferred direction.

We summarize the results of all simulations in the diagrams shown in Fig. 18. The aim is to show that the features presented in Sections 3.1–3.5 are stable over ranges of parameters and random realizations. In the left panels of Fig. 18, the x-axis is the inverse of strength excess $1/S$, which is representative of the state of shear stress load of the fault, with large $1/S$ values meaning high relative stress. The x-axis of the right panels is the dissimilarity of peak slip velocity distributions δV_{max} (eq. 4) as a measure of the difference in slip history introduced by the material contrast. The y-axis of the top panels shows the relative difference in PGV, which is the anologous measure concerning the ground motion, whereas the y-axis for the bottom panels, the moment magnitude M_W, shows the total slip for each event for each pair of simulations. Each coloured triangle represents the occurrence of one of the six modes listed earlier. The direction of the triangles point into the preferred direction of each simulation. Hence, each triangle pointing to the left represents the occurrence of a specific propagation mode for a Λ_L-simulation, whereas each triangle pointing to the right represents the occurrence of this specific propagation mode for a Λ_R-simulation. The simulations for a given pair with reversed orientations (Λ_L, Λ_R)

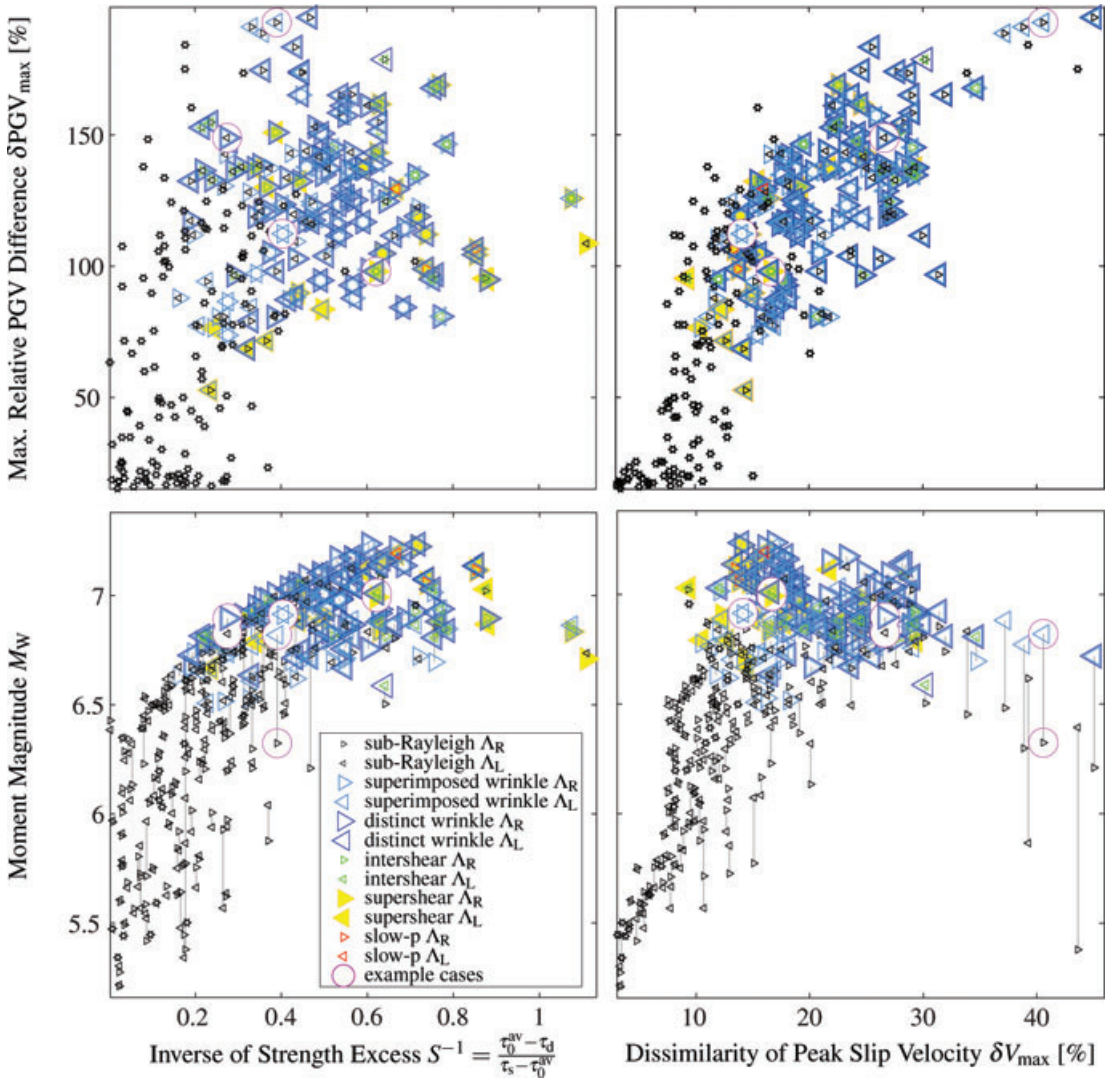

Figure 18. Summary showing the occurrence of the six possible propagation modes, as a function of inverse of strength excess, dissimilarity of peak slip velocity, moment magnitude, and maximum relative PGV difference for 266 simulation pairs.

have in general different moment magnitudes, hence the symbols for the two orientations split up spatially and a simulation pair is connected with a grey line. Otherwise, the symbols appear on top of each other. Since for all of our simulated cases rupture starts propagating spontaneously in the sub-Rayleigh range (mode i) we do not display the corresponding symbol (black triangle) when at least one of the other modes (ii−vi) shows up in addition.

The examples discussed in Sections 3.1–3.4 are highlighted and isolated by the magenta circles in Fig. 18. Of course the rest of the 266 simulation pairs also comprise other combinations of effects and/or propagation modes than the ones in the four examples, hence there are symbol combinations that we do not explicitly discuss as for the examples in the previous sections. Yet, all propagation modes are nicely shown in those four examples. The only exception is the mode that is represented by a red triangle, which stands for propagation close to the *P*-wave velocity of the softer medium in the non-preferred direction. In Example 4 (supershear, Section 3.4) there is actually some small area (red shaded area in Fig. 16) that indicates such propagation, though it is below our chosen threshold. Simulations that showed slightly larger area percentage with $v_r = v_P^{slow} \pm 3\%$ existed only in very few cases. When supershear propagation occurred it stayed mostly below the velocity of the slow *P*-wave v_P^{slow}.

The plots in Fig. 18 provide several tendencies in the results of our parameter space study, though clear systematic trends remain difficult to retrieve. Here we discuss some general findings that exist within the tested model and parameter limits.

Superimposed wrinkle-like slip pulses travelling in the preferred direction close to the generalized Rayleigh velocity nucleate naturally for a large number of events. Very often the ruptures become even predominant wrinkle-like pulses. There are events that become supershear for one orientation, whereas staying sub-Rayleigh in the reversed configuration. Also there are several cases similar to Example 4 (Section 3.4), where two rupture phases, a supershear and a wrinkle-like pulse, propagate for one material contrast orientation, whereas there is mainly supershear propagation in the simulation with reversed situation.

Inside the parameter-space tested here, small events ($M_W \approx 5.3$–6.5) never develop wrinkle-like pulses (no blue triangle in the lower half of the plots, see Fig. 18 bottom panels). We think that this has

© 2009 The Authors, *GJI*, **178,** 921–938
Journal compilation © 2009 RAS

its origin in too small propagation distances from the instantaneous nucleation patch. In other words, we believe that those events that developed a wrinkle-pulse are not large because of the wrinkle-like pulse, but that they could develop the wrinkle-like phenomenon because of a large enough propagation distance. This is what is expected from the results of Rubin & Ampuero (2007). The situation might change if the nucleation procedure would include dynamic bimaterial effects, which would be more realistic.

Supershear rupture occurs only in cases of relatively large moment magnitude $M_W > 6.7$ (see Fig. 18 bottom panels, yellow triangles). In contrast to the wrinkle-like propagation mode, supershear often occurs in the early stage of a rupture (which can thus be used as a prediction for a large event in our model). Whether supershear rupture is initiated around the nucleation zone or further away, it generally involves an area where initial shear stress is relatively high even though its average might be rather low (inverse of strength excess small: $1/S \approx 0.25$).

In Fig. 18, one can note that for the majority of simulation pairs that have not developed wrinkle-like propagation modes for at least one of the orientations (Λ_L, Λ_R), the relative difference in ground motion is, on average, smaller than for the couples for which at least one orientation developed the wrinkle-pulse (see top panels: more points with two black triangles—which appear as a star—are in the lower half with $\delta\text{PGV}_{max} < 110\%$ than in the upper half $\delta\text{PGV}_{max} > 110\%$). Nevertheless Fig. 18 exhibits many examples with no wrinkle-mode or supershear-mode of propagation throughout the entire range of δPGV, and there are also many examples that exhibit a large difference in propagation mode (e.g. superimposed and/or distinct Weertman pulse for Λ_L and sub-Rayleigh for Λ_R) but a medium difference in ground motion ($70\% < \delta\text{PGV}_{max} < 110\%$). Even very large differences in peak-ground motion (δPGV, δPGA) are possible when the dominant propagation mode is sub-Rayleigh (cases with two black triangles in the range of high $\delta\text{PGV} \geq 150\%$).

In most of the simulation pairs with a large dissimilarity of peak slip velocity, $\delta V_{max} > 20\%$, a wrinkle-like pulse of slip is involved for one orientation of the material contrast, whereas it is not in the reversed configuration (see Fig. 18 right panels, the cases with a blue triangle in one direction only). There are few cases with large dissimilarity of peak slip velocity although both simulations of a pair are essentially in the sub-Rayleigh range of propagation velocity (see Fig. 18 right bottom panel, simulation pairs represented by two black triangles). However, in those cases the difference in moment magnitudes is also large and hence these are cases where rupture could slowly overcome asperities of low initial shear stress and renucleate large additional portions of the fault in one material configuration only, like in Example 2 (different magnitude—Section 3.2), but staying sub-Rayleigh here.

As mentioned earlier, our model has a lower limit of event size due to the nucleation patch ($M_W^{min} \approx 5.3$) and an upper limit ($M_W^{max} \approx 7.2$) due to the size of the fault. We demonstrated in Example 3 (wrinkle-like pulse—Section 3.3) that the wrinkle-mode can be very efficient in overcoming larger distances of relatively low initial shear stress once such a mode of propagation is initiated. Contrary to the usual modes of ruptures, these wrinkle pulses are not easily stopped by the artificially low initial stresses of the tapering regions near the boundaries; often such still well developed pulses reached the unbreakable barrier. Hence those ruptures appear to be potential candidates for large earthquakes ($M_W > 7.2$) in a spatially extended fault model of the same kind. However, we do not accomplish such an extension in the study presented here.

3.7 Summary of results

We found a range of realistic parameters for that nucleated earthquakes essentially develop as classical cracks with no development of a superimposed or distinct wrinkle-like Weertman pulse or supershear rupture propagation and with no large differences in final slip, as in Andrews & Harris (2005). Nevertheless the seismic radiation differs substantially for many of those cases between the bimaterial orientations, leading to differences in strong ground motion due to different slip histories (this possibility has been mentioned by Andrews & Harris 2005).

For another range of realistic parameters we found a transformation of rupture during propagation from an initially crack-like propagation into an enlarging crack with a superimposed wrinkle-like pulse. Although seismic radiation differs for the switched bimaterial orientations, final slip does not change significantly in this case. On average these cases show larger differences in ground motion than the previous cases.

For yet other sets of realistic parameters we found that ruptures start like classical cracks, then slowly break stress barriers (areas of lower stress) only in the preferred direction (Λ), then trigger a secondary event at an area of high stress. This leads to differences of earthquake magnitudes and a strong directivity. In these cases only early phases of the ground motion are comparable between the two bimaterial orientations. The secondary events have the potential to develop wrinkle-like propagation modes since they start already unilaterally in the preferred direction, although a limiting factor is the size of the fault. Peak ground motions are orders of magnitude different. We therefore presume that the bimaterial mechanism is important for earthquake dynamics as well as for earthquake hazard and damage.

We also found sets of realistic parameters where rupture transforms to a mainly wrinkle-like pulse. Seismic radiation can be very different in these cases when switching materials. These pulses often overcome additional areas of low initial shear stress. Thus, it provides a potential mechanism to trigger additional ruptures further along strike in the preferred direction beyond the limited fault size used in this study, where these ruptures are always stopped ultimately at the model boundary.

We finally found situations where supershear propagation occurred. In many cases the bimaterial mechanism prevents rupture from becoming supershear in the preferred direction, whereas supporting it in the opposite direction. Also, there are cases with a supershear propagation at the rupture tip and a superimposed wrinkle-like slip pulse travelling behind the rupture tip at the generalized Rayleigh velocity in the favoured direction. In these cases peak amplitudes of ground motion can split up in time. Such ground motion has been interpreted as supershear transients in real earthquakes, for example for the 2002 Denali fault earthquake (Dunham & Archuleta 2004), and are not restricted to bimaterial interfaces.

4 DISCUSSION

Geological fault-zone structures are thought to be complex systems on all scales, and realistic models of earthquake rupture are thought to involve a large number of physical mechanisms, for example off-fault energy dissipation due to plastic strain (Andrews 2005), visco-elasticity, melt lubrication (Di Toro *et al.* 2006), thermal pressurization (Bizzarri & Cocco 2006a,b), flash heating (Rice 2006), poroelasticity (Dunham & Rice 2008), etc. We exclude all those effects and use a simple planar frictional interface governed by slip-weakening friction and a heterogeneous initial shear stress.

In such a model all physical processes on the fault are projected into the friction laws and/or into the heterogeneous stress, which together might mimic realistic macroscopic behaviour of the fault. Therefore, there is the possibility that many different effects, not considered in this work, may counterbalance (or enhance) the bimaterial mechanism and therefore hinder (or support) the generation of propagation modes we found.

For instance, Rudnicki & Rice (2006) developed a poroelastic fault-zone model which has been explored by Dunham & Rice (2008). A mismatch in poroelastic properties across faults may lead to a similar response as a mismatch in elastic parameters across the fault (normal stress reductions/increases). The elastic and the poroelastic effects enhance each other for the case that the compliant side is more permeable, whereas they oppose each other for the case that the stiff side is more permeable. In the range of representative contrasts of natural faults (10% contrast of elastic parameters, and a factor-of-ten contrast of permeability) both effects have comparable magnitudes (Dunham & Rice 2008).

Our model is purely elastic in the bulk and therefore does not account for dissipative processes and damage. With such a purely elastic response in the bulk our results are likely biased when comparing to more realistic geological models due to the lack of dissipative processes and damage. Such more realistic models are beyond the scope of this study. However, we calculated strength of rock assuming typical laboratory derived parameters for intact rock (e.g. Schellart 2000, table 1), for Example 4 (supershear) with a transition of wrinkle-like propagation and supershear burst, and found that stresses stay below strength in the bulk for some materials (e.g. marble or limestone) whereas stresses exceed the limits for others (e.g. granite, gabbro) [an example is shown in the Supporting Information (SI 16)]. Clearly the role of damage should be investigated in future studies of bimaterial strike-slip faults.

Rice (2006) argues that there should exist some additional weakening mechanism(s). Otherwise, in view of the small thickness of the shear zone, melting would essentially always occur for typical slip velocities and rise times, which is not observed on exhumed faults. However, note that most earthquake simulations performed so far in the literature fall into this unrealistic category.

However, in the context of modelling earthquake scenarios with dynamic source models and a simple weakening mechanism of the frictional interface (e.g. slip-weakening friction) between elastic half-spaces, our study shows that the presence of a material contrast can significantly alter slip history on the fault, hence can diversify resulting wave-effects at the free surface. These should be taken into account in estimates of peak ground motion. In fact, kinematic features specific of bimaterial dynamics (like strong directivity related to the Weertman pulse preferred direction, as shown here) might need to be incorporated into earthquake scenario simulations with kinematic source models.

In all our simulations we found that the rupture had to propagate a certain distance before it could develop characteristics of the Weertman pulse (e.g. $v_r = v_{gr}$, self-sharpening, self-amplifying behaviour). This suggests that the wrinkle-modes of rupture on bimaterial interfaces is more significant for large earthquakes after large propagation distances. However, in our instantaneous nucleation procedure, dynamic bimaterial effects are not accounted for. This introduces a lower limit for earthquake sizes which are affected by the bimaterial mechanism. Hence its contribution might be underestimated for small earthquakes in our study.

We noted that in cases where the rupture propagation velocity is not close to the generalized Rayleigh velocity, the slip history is altered significantly, leading to large differences in ground motion, when switching materials. Thus, it is not necessary to nucleate Weertman-like pulses in order for the bimaterial mechanism to alter the dynamic behaviour on the fault.

Once a Weertman pulse is nucleated, it shows self-sharpening and self-amplifying behaviour. This makes it difficult to come to grid-independent solutions for all involved field variables on a detailed scale. However, the goal of this study is not a detailed investigation of the wrinkle-like pulse itself, but to qualitatively estimate rupture histories on a bimaterial strike-slip fault and the resulting ground motion. It would have consumed an enormous amount of computation time if we had refined our simulation as we did in our previous paper (Brietzke *et al.* 2007). We did some simulations with a few levels of grid refinement and observed similar features. An example for such a test is shown in the Supporting Information (SI 15). So we decided to perform most of our simulations with a rather coarse grid-size. Higher numerical resolutions are of course desirable, but we are nevertheless confident that the various tendencies and features reported here are robust and that the conclusions of the paper are qualitativly identical with refined simulations, leaving the overall picture of results unchanged.

The tapering of shear stress to the fault edges and the unbreakable boundary at the fault edge cause every rupture to ultimately stop. As for real ruptures this results in a very strong seismic radiation at the fault edges for the case of a rupture front with large amplitude hitting the tapered region (or even the unbreakable boundary). This enhances peak ground motion at the vicinities of the fault. However, the tapering region can be seen as another stress heterogeneity present in both material configurations (Λ_L, Λ_R).

A common feature for many individual model realizations tested in this study is a non-symmetric propagation velocity, with generalized Rayleigh velocity into the preferred direction and supershear propagation in the unfavoured direction. Such propagation is also observed in laboratory experiments by Xia *et al.* (2005), as well as in other numerical studies (e.g. Shi & Ben-Zion 2006). In the case of a constant friction coefficient (Coulomb friction) the non-symmetric propagation is restricted to the two explicit propagation modes: (1) the Weertman pulse in the preferred direction with $v_r = v_{gr}$, and (2) the slow-P pulse associated $v_r = v_P^{slow}$ (Cochard & Rice 2000). It has been discussed by Xia *et al.* (2005) that the 1999 $M_W = 7.4$ Izmit earthquake and the 1999 $M_W = 7.2$ Düzce earthquake are potential candidates for such a bimaterial-typical propagation behaviour, with supershear propagation in one direction only, that is towards the east (Bouchon *et al.* 2001). Both of these events happened along the northern branch of the NNAF. To explain the asymmetric propagation of the two events with the bimaterial favouring, the southern side of the NNAF must have slower seismic velocities than the northern side of the NNAF. We are not aware of any detailed model of seismic velocities in that region, but there is evidence that the south side of the NNAF has slower seismic velocities: deformation inferred from coseismic and early postseismic SAR interferometry (Cakir *et al.* 2003) as well as from GPS data (Flerit *et al.* 2003) both indicate larger deformation on the south side. Therefore, a velocity contrast across the NNAF, its slower side being the south side, is very likely. And our results are consistent with the laboratory experiments of Xia *et al.* (2005) and with the observations of asymmetric rupture propagation at the Izmit and Düzce earthquakes. However, a refracted arrival recorded close to the eastern edge of the 1999 Izmit rupture gives evidence that the material on the northern side might instead be the slower side (see discussion in Bouchon *et al.* 2001; Andrews 2002).

Another fault that has often been mentioned in connection with bimaterial rupture propagation is the Parkfield section of the San

© 2009 The Authors, *GJI*, **178,** 921–938
Journal compilation © 2009 RAS

Andreas fault. There, the velocity structure is well known to have a moderate velocity contrast across the fault, its slow side being the continental side. Hence the preferred rupture direction in the subshear range at Parkfield is to the southeast. Nevertheless, whereas the 1966 earthquake indeed propagated to the southeast, the recent 2004 $M_W = 6$ event ruptured mainly in the dynamically unpreferred northwest direction. Some authors take this as evidence that material contrast is not relevant for earthquake source dynamics, and that the propagation direction cannot be predicted (e.g. Andrews & Harris 2005; Harris & Day 2005). However, it seems clear that material contrast is not the only factor that influences rupture dynamics, and we agree with Ben-Zion (2006a,b) that the propagation direction can only be predicted in a statistical sense. For example, if the nucleation zone is close to a barrier, there is only one direction for the earthquake to rupture, whether it be the favoured or the unfavoured direction! Custódio & Archuleta (2007) compare the 1966 and 2004 Parkfield earthquakes. The hypocentres of both events are in different locations; also, the large difference in aftershock locations of the 1966 (Eaton *et al.* 1970) and the 2004 (Thurber *et al.* 2006) Parkfield events show that the events did not only rupture in different directions, but ruptured different areas of the fault. Such variability is to be expected within an area of heterogeneous stress, which is thought to be the rule rather than the exception, and we would need to know the state of stress more precisely to be able to quantitatively estimate the relative contribution of the various factors. The results of our simulations also show considerable variability, all of which being due to the heterogeneity in the initial stress field, and they are certainly consistent with the two Parkfield events.

Besides, even if the rupture extent and direction of the 2004 event is not controlled by the material contrast, the radiated ground motion may still have been considerably influenced by the bimaterial dynamics, similar to what we show in our study (e.g. Example 1, Fig. 4). Also, even though the 2004 rupture mainly propagated to the northwest, there has been some propagation to the southeast; there were accelerometer stations close to the southeastern edge of the fault which recorded large amplitudes in ground motion, especially for the fault normal component [see for example Shakal *et al.* (2006), Liu *et al.* (2006)], which is a characteristic feature of bimaterial rupture. This has been demonstrated by Ma *et al.* (2008) who compared synthetics of their dynamic source modelling and trial-and-error inversion of the 2004 Parkfield event with near fault strong ground motion recordings. Their 'best' model provided a remarkable fit to the observations spawning notable amplification of slip velocity and ground motion to the southeast, the dynamically favoured direction.

Let us end this part with a highly speculative guess: the fact that the 2004 Parkfield event happened more than a decade later than predicted could be interpreted as being harder to nucleate an event in the non-preferred direction.

Earthquakes on a bimaterial interface are also suspect of causing non-symmetric aftershock distributions. Rubin & Ampuero (2007) simulated bimaterial 2-D in-plane ruptures with regularized slip-weakening friction and force them to stop at stress barriers after some propagation distance along the fault. They find different behaviours of stopping for the dynamically favoured and unfavoured directions that can explain asymmetric aftershock distributions of bimaterial faults as has been observed by Rubin & Gillard (2000) and Rubin (2002). As in our simulations, Rubin & Ampuero (2007) observe that under certain conditions bimaterial slip pulses propagate into stress barriers much further than regular rupture modes. This is due to the tensile perturbation of normal stress that carries the bimaterial pulse of slip. Rubin & Ampuero (2007) showed that this effect smoothes the stress concentrations at the edge of the fault in the dynamically preferred direction. Our results verify the estimation that generation of pulses is not inhibited in the 3-D case with a heterogeneous stress distribution (Rubin & Ampuero 2007). We found that also in our 3-D-model with heterogeneous shear stress, pulses of slip are generated and travel far into stress barriers, smoothing out and significantly reducing amplitudes of stress concentration at the fault edges.

Ampuero & Ben-Zion (2008) studied in-plane ruptures on a bimaterial fault governed by a regularized strongly velocity-weakening friction. They showed that for a wide range of parameters large scale pulses travelling into the preferred direction are also possible, and small scale pulses (scale of the process zone) can detach from the rupture front also travelling into the preferred direction, the latter being dependent on the relaxation scale of the regularization. They also found asymmetric bilateral crack-like propagation within another range of parameters and tried to analyse the asymmetry in seismic potency of their events in a statistical sense. In our study, we do not have a velocity-weakening model and no large scale pulses are generated (aside from ruptures becoming pulse-like events due to stopping phases radiating from the fault boundaries in our 3-D model setup). However, all our results are consistent with the results of Ampuero & Ben-Zion (2008). We agree with Ampuero & Ben-Zion (2008) that it is important to clarify effects of the bimaterial mechanism on earthquake rupture propagation with additional theoretical studies, and test the associated predictions with detailed field and laboratory observations.

5 CONCLUSIONS

We performed a numerical investigation of dynamic ruptures on a bimaterial interface in 3-D with regularized slip-weakening friction and a heterogeneous initial shear stress and discussed the resulting strong ground motion. We showed that for many parameter sets the dynamics of rupture propagation are significantly influenced by the broken symmetry due to the material discontinuity during rupture propagation. Large differences in peak ground motion (PGV and PGA) are possible when changing the orientation of the material contrast even when slip-distribution of the individual events are very similar.

Wrinkle-like slip pulse specific to the bimaterial mechanism nucleates naturally from initially crack-like propagation of rupture when the involved parameters allowed for large propagation distances. Once such a pulse is generated it appears to have high potential to overcome large distances within areas of relatively low initial shear stress. It also appears that the existence of a wrinkle-like slip pulse impedes the initiation of supershear propagation in the preferred direction. For those cases where supershear is nevertheless initiated, a secondary superimposed wrinkle pulse propagating at the generalized Rayleigh velocity is often nucleated behind the rupture front. By contrast, supershear propagation seems to be promoted in the unfavoured direction.

The dynamic weakening of the fault due to the normal stress alteration during slip is also efficient in the range of small propagation velocities. In such cases, secondary events are triggered and the orientation of the material contrast determines rupture extent and the size of the earthquake, potentially by orders of magnitude.

The variety of propagation modes investigated in this study is consistent with laboratory experiments, thorough numerical investigation, as well as with crustal earthquake observations.

Therefore our main conclusions are as follows:

(1) The influence of a material contrast on final slip may be small, nevertheless—as shown in this study and envisioned by Andrews & Harris (2005)—the effect on the surface ground motion and earthquake hazard can be substantial.

(2) Our simulations contradict the conclusion of previous studies ('The wrinkle-like slip pulse is not important in earthquake dynamics' Andrews & Harris 2005). We find that for a broad range of realistic parameters, the wrinkle-mode of propagation is an attractive propagation mode of rupture. When such pulses are generated, earthquake rupture dynamics is strongly influenced by the wrinkle-like slip pulse characteristic of bimaterial interfaces. The resulting effect on ground motion may be very large.

(3) It is not necessary that a wrinkle-like pulse (or Weertman pulse) be generated to significantly alter slip history. The bimaterial mechanism can affect rupture dynamics throughout the entire range of seismic propagation velocity (from sub-Rayleigh to supershear) and might even support very slow modes of propagation, the latter obviously needing deeper investigation.

ACKNOWLEDGMENTS

We would like to thank the Leibniz–Rechenzentrum (LRZ) for providing parallel computing facilities used in this study and the KONWIHR project for the financial support. We would like to thank František Gallovič for discussions. AC also thanks Renaud Toussaint for discussions. We would like to thank Jens Oeser who did a great job on administrating the local workstation PCs and the local files-system needed for the large data sets produced in this study. We also thank the Human Resources and Mobility Program (MCRTN-SPICE). We thank also the reviewers Jean-Paul Ampuero and Eric Dunham who criticized the manuscript very constructively.

REFERENCES

Adams, G.G., 1995. Self-excited oscillations of two elastic half-spaces sliding with a constant coefficient of friction, *ASME J. Appl. Mech.,* **62,** 867–872.

Ampuero, J.-P. & Ben-Zion, Y., 2008. Cracks, pulses and macroscopic asymmetry of dynamic rupture on a bimaterial interface with velocity-weakening friction, *Geophys. J. Int.,* **173**(2), 674–692.

Ampuero, J.P. & Dahlen, F.A., 2005. Ambiguity of the Moment Tensor, *Bull. seism. Soc. Am.,* **95**(2), 390–400.

Andrews, D.J., 1976. Rupture velocity of plane strain shear cracks, *J. geophys. Res.,* **81**(32), 5679–5689.

Andrews, D.J., 2002. Comment on 'how fast is rupture during an earthquake? New insights from the 1999 turkey earthquake', *Geophys. Res. Lett.,* **29**(15), 1714.

Andrews, D.J., 2005. Rupture dynamics with energy loss outside the slip zone, *J. geophys. Res.,* **110,** B01307.

Andrews, D.J. & Ben-Zion, Y., 1997. Wrinkle-like slip pulse on a fault between different materials, *J. geophys. Res.,* **102,** 553–572.

Andrews, D.J. & Harris, R.A., 2005. The wrinkle-like slip pulse is not important in earthquake dynamics, *Geophys. Res. Lett.,* **32,** L23303.

Ben-Zion, Y., 2006a. A comment on 'The wrinkle-like slip pulse is not important in earthquake dynamics' by Andrews and Harris, *Geophys. Res. Lett.,* **33,** L06310.

Ben-Zion, Y., 2006b. A comment on 'Material contrast does not predict earthquake rupture propagation direction' by Harris and Day, *Geophys. Res. Lett.,* **33,** L13310.

Ben-Zion, Y. & Andrews, D.J., 1998. Properties and implications of dynamic rupture along a material interface, *Bull. seism. Soc. Am.,* **88**(4), 1085–1094.

Ben-Zion, Y. & Huang, Y., 2002. Dynamic rupture on an interface between a compliant fault-zone layer and a stiffer surrounding solid, *J. geophys. Res.,* **107,** 2042.

Bizzarri, A. & Cocco, M., 2006a. A thermal pressurization model for the spontaneous dynamic rupture propagation on a three-dimensional fault, 1: Methodological approach, *J. geophys. Res.,* **111,** B05303.

Bizzarri, A. & Cocco, M., 2006b. A thermal pressurization model for the spontaneous dynamic rupture propagation on a three-dimensional fault: 2. traction evolution and dynamic parameters, *J. geophys. Res.,* **111,** B05304.

Bouchon, M., Bouin, M.-P., Karabulut, H., Toksöz, M.N., Dietrich, M. & Rosakis, A.J., 2001. How fast is rupture during an earthquake? New insights from the 1999 turkey earthquakes, *Geophys. Res. Lett.,* **28**(14), 2723–2726.

Brietzke, G.B. & Ben-Zion, Y., 2006. Examining tendencies of in-plane rupture to migrate to material interfaces, *Geophys. J. Int.,* **167**(2), 807–819.

Brietzke, G.B., Cochard, A. & Igel, H., 2007. Dynamic rupture along bimaterial interfaces in 3-D, *Geophys. Res. Lett.,* **34,** L11305.

Cakir, Z., de Chabalier, J.-B., Armijo, R., Meyer, B., Barka, A. & Peltzer, G., 2003. Coseismic and early post-seismic slip associated with the 1999 Izmit earthquake (Turkey), from SAR interferometry and tectonic field observations, *Geophys. J. Int.,* **155,** 93–110.

Cochard, A. & Rice, J.R., 2000. Fault rupture between dissimilar materials: ill-posedness, regularization, and slip-pulse response, *J. geophys. Res.,* **105,** 25 891–25 908.

Collino, F. & Tsogka, C., 2001. Application of the perfectly matched absorbing layer model to the linear elastodynamic problem in anisotropic heterogeneous media, *Geophysics,* **66**(1), 294–307.

Custódio, S. & Archuleta, R.J., 2007. Parkfield eathquakes: characteristic or complementary?, *J. geophys. Res.,* **112,** B05310.

Dalguer, L.A. & Day, S.M., 2007. Staggered-grid split-node method for spontaneous rupture simulation, *J. geophys. Res.,* **112,** B02302.

Di Toro, G., Hirose, T., Nielsen, S. & Pennacchioni, G., Shimamoto, S., 2006. Natural and experimental evidence of melt lubrication of faults during earthquakes, *Science,* **311,** 647–649.

Dor, O., Ben-Zion, Y., Rockwell, T.K. & Brune, J., 2006. Pulverized rocks in the Mojave section of the San Andreas fault zone, *Earth planet. Sci. Lett.,* **245,** 642–654.

Dor, O., Yildirim, C., Rockwell, T.K., Ben-Zion, Y., Emre, O., Sisk, M. & Duman, T.Y., 2008. Geologic and geomorphologic asymmetry of the 1943 and 1944 earthquakes on the North Anatolian Fault: possible signals for preferred earthquake propagation direction., *Geophys. J. Int.,* **173,** 483–504.

Dunham, E.M. & Archuleta, R.J., 2004. Evidence for a supershear transient during the 2002 denali fault earthquake, *Bull. seism. Soc. Am.,* **94**(6B), 256–268.

Dunham, E.M. & Rice, J.R., 2008. Earthquake slip between dissimilar poroelastic materials, *J. geophys. Res.,* **113,** B09304.

Eaton, J.P., O'Neil, M.E. & Murdock, J.N., 1970. Aftershocks of t the 1966 Parkfield-Cholame, California, earthquake: a detailed sudy, *Bull. seism. Soc. Am.,* **60,** 1151–1197.

Flerit, F., Armijo, R., King, G.C.P., Meyer, B. & Barka, A., 2003. Slip partitioning in the Sea of Marmara pull-apart determined from GPS velocity vectors, *Geophys. J. Int.,* **154,** 1–7.

Harris, R.A. & Day, S.M., 1997. Effect of a low-velocity zone on a dynamic rupture, *Bull. seism. Soc. Am.,* **87,** 1267–1280.

Harris, R.A. & Day, S.M., 2005. Material contrast does not predict earthquake rupture propagation direction, *Geophys. Res. Lett.,* **32,** L23301.

Levander, A.R., 1988. Fourth-order finite-difference P−SV seismograms, *Geophysics,* **53**(11), 1425–1436.

Liu, P., Custodio, S. & Archuleta, R.J., 2006. Kinematic inversion of the 2004 m 6.0 parkfield earthquake including an approximation to site effects, *Bull. seism. Soc. Am.,* **96,** S143–S158.

Ma, S., Custodio, S., Archuleta, R.J. & Liu, P., 2008. Dynamic modeling of the 2004 M_w 6.0 Parkfield, California, earthquake, *J. geophys. Res.,* **113,** B02301.

Mai, P.M. & Beroza, G.C., 2002. A spatial random-field model to characterize complexity in earthquake slip, *J. geophys. Res.,* **107**(B11), 2308, doi:10.1029/2001jb000588.

Marcinkovich, C. & Olsen, K., 2003. On the implementation of perfectly matched layers in a three-dimensional fourth-order velocity-stress finite difference scheme, *J. geophys. Res.,* **108**(B5), 2276.

Prakash, V., 1998. Frictional response of sliding interfaces subjected to time varying normal pressures, *J. Tribol.,* **120,** 97–102.

Prakash, V. & Clifton, R.J., 1993. Time resolved dynamic friction measurements in pressure-shear, *Appl. Mech. Div.,* **165,** 33–48.

Ranjith, K. & Rice, J., 2001. Slip dynamics at an interface between dissimilar materials, *J. Mach. Phys. Solids,* **49,** 341–361.

Rice, J.R., 2006. Heating and weakening of faults during earthquake slip, *J. geophys. Res.,* **111,** B05311.

Ripperger, J., Ampuero, J.P., Mai, P.M. & Giardini, D., 2007. Earthquake source characteristics from dynamic rupture with constrained stochastic fault stress, *J. geophys. Res.,* **112,** B04311.

Rubin, A.M., 2002. Aftershocks of microearthquakes as probes of the mechamics of rupture, *J. geophys. Res.,* **107**(B7), 2142.

Rubin, A.M. & Ampuero, J.P., 2007. Aftershock asymmetry on a bimaterial interface, *J. geophys. Res.,* **112,** B05307.

Rubin, A.M. & Gillard, D., 2000. Aftershock asymmetry/rupture directivity among central San Andreas fault microearthquakes, *J. geophys. Res.,* **105**(B8), 19 095–19 109.

Rudnicki, J.W. & Rice, J.R., 2006. Effective normal stress alteration due to pore pressure changes induced by dynamic slip propagation on a plane between dissimilar materials, *J. geophys. Res.,* **111,** B10308.

Schellart, W.P., 2000. Shear test results for cohesion and friction coefficients for different granular materials: scaling implications for their usage in analogue modelling, *Tectonophysics,* **324,** 1–16.

Shakal, A., Haddadi, H., Graizer, V., Lin, K. & Huang, M., 2006. Some Key Features of the strong-motion data from the M 6.0 parkfield, California, Earthquake of 28 September 2004, *Bull. seism. Soc. Am.,* **96**(4b), 90–118.

Shi, Z. & Ben-Zion, Y., 2006. Dynamic rupture on a bimaterial interface governed by slip-weakening friction, *Geophys. J. Int.,* **165,** 469–484.

Smith, D.E., 2006. A new paradigm for interpreting stress inversions from focal mechanisms: how 3-D stress heterogeneity biases the inversions toward the stress rate, *PhD thesis*, California Institute of Technology, Pasadena.

Thurber, C., Zhang, H., Waldhauser, F., Hardebeck, J., Michael, A. & Eberhart-Phillips, D., 2006. Three-dimensional compressional wavespeed model, earthquake relocations, and focal mechanisms for the Parkfield, California, region, *Bull. seism. Soc. Am.,* **96,** S38–S49.

Weertman, J.J., 1980. Unstable slippage across a fault that separates elastic media of different elastic constants, *J. geophys. Res.,* **85,** 1455–1461.

Xia, K., Rosakis, A.J., Kanamori, H., & Rice, J.R., 2005. Laboratory earthquakes along inhomogeneous faults: directionality and supershear, *Science,* **308,** 681–684.

SUPPORTING INFORMATION

Additional Supporting Information may be found in the online version of this article.

Appendix S1.

Please note: Wiley-Blackwell are not responsible for the content or functionality of any supporting materials supplied by the authors. Any queries (other than missing material) should be directed to the corresponding author for the article.